Chemical Science

ROYAL SOCIETY OF CHEMISTRY

REVIEW

View Article Online
View Journal | View Issue

Cite this: *Chem. Sci.*, 2021, **12**, 4267

Defective TiO_2 for photocatalytic CO_2 conversion to fuels and chemicals

Sushma A. Rawool, Kishan K. Yadav and Vivek Polshettiwar *

Photocatalytic conversion of CO_2 into fuels and valuable chemicals using solar energy is a promising technology to combat climate change and meet the growing energy demand. Extensive effort is going on for the development of a photocatalyst with desirable optical, surface and electronic properties. This review article discusses recent development in the field of photocatalytic CO_2 conversion using defective TiO_2. It specifically focuses on the different synthesis methodologies adapted to generate the defects and their impact on the chemical, optical and surface properties of TiO_2 and, thus, photocatalytic CO_2 conversion. It also encompasses theoretical investigations performed to understand the role of defects in adsorption and activation of CO_2 and identify the mechanistic pathway which governs the formation and selectivity of different products. It is divided into three parts: (i) general mechanism and thermodynamic criteria for defective TiO_2 catalyzed CO_2 conversion, (ii) theoretical investigation on the role of defects in the CO_2 adsorption–activation and mechanism responsible for the formation and selectivity of different products, and (iii) the effect of variation of physicochemical properties of defective TiO_2 synthesized using different methods on the photocatalytic conversion of CO_2. The review also discusses the limitations and the challenges of defective TiO_2 photocatalysts that need to be overcome for the production of sustainable fuel utilizing solar energy.

Received 24th November 2020
Accepted 20th January 2021

DOI: 10.1039/d0sc06451c

rsc.li/chemical-science

1. Introduction

Extensive use of fossil fuels leads to the depletion of natural resources and is a major source of anthropogenic CO_2. Hence, there is an active search going on for the replacement of fossil fuels with renewable energy sources.[1,2] According to the International Panel on Climate Change (IPCC) prediction, by 2100, the global temperature may rise by 1.9 °C, due to continuous increase in anthropogenic CO_2.[3] Thus, CO_2 capture, utilization, and storage are key in reducing its increased concentration in the earth's atmosphere. The use of solar energy, an abundant and renewable source of energy available on the earth, is one of the best solutions to tackle energy challenges. The total solar energy falling on the earth is 1.3×10^5 TW, which is four orders of magnitude higher than the current

Department of Chemical Sciences, Tata Institute of Fundamental Research (TIFR), Mumbai, India. E-mail: vivekpol@tifr.res.in; Tel: +91 8452886556

Dr. Sushma A. Rawool received her Ph.D. degree from the Homi Bhabha National Institute (HBNI) Mumbai under the supervision of Dr Mrinal Pai at Bhabha Atomic Research Center (BARC), Mumbai, in 2018. She is currently working as a post-doctoral visiting fellow at Tata Institute of Fundamental Research (TIFR), Mumbai, in Prof. Vivek Polshettiwar's nanocatalysis group. Her research interests focus on the design and synthesis of nanomaterials for their application in photocatalytic H_2 generation and CO_2 conversion.

Mr. Kishan K. Yadav received his master's degree from Banaras Hindu University in 2018 and is currently pursuing his PhD at Tata Institute of Fundamental Research (TIFR), Mumbai. He worked in Prof. Vivek Polshettiwar's nanocatalysis group and studied defective TiO_2 for photocatalytic CO_2 conversion. His research interests focus on photocatalytic reactions and spectroscopic studies.

overall human energy consumption (1.85 × 10 TW in 2017). Conversion of inexhaustible solar energy into renewable energy carriers such as electricity using solar cells or hydrogen generated by photocatalytic water splitting is a promising approach. However, the storage of the renewable electricity generated from solar cells, as well as hydrogen gas, is challenging, preventing the development of these technologies.

The catalytic conversion of CO_2 to fuels and chemicals using solar energy can provide a solution to excessive anthropogenic CO_2 in the atmosphere as well as an alternative to the storage of electricity or hydrogen gas. Photocatalytic CO_2 conversion offers a viable solution for the abatement of climate change by converting CO_2 into valuable fuels using solar energy.[4–8] The use of CO_2 from the atmosphere as a carbon source and its conversion into the hydrocarbons (fuel) which can be further utilized as an energy source in a closed-loop is often termed as 'artificial photosynthesis'.[9]

The first report on photocatalytic CO_2 reduction came in 1978 by Halmann *et al.*[10] They studied the photoelectrochemical conversion of CO_2 to formic acid, formaldehyde, and methane under UV-visible light illumination using single crystal gallium phosphide. In 1979, Inoue *et al.*[11] reported the generation of organic compounds like formic acid, formaldehyde, methanol and methane by photocatalytic CO_2 conversion using an aqueous suspension of different semiconductors such as WO_3, TiO_2, CdS, GaP, SiC, and ZnO under UV-visible light illumination.[11] After these initial discoveries, although a large number of photocatalysts have been explored, the desired productivity, selectivity, and catalyst stability have not yet been achieved.

The efficiency of the photocatalytic processes lies in the development of a suitable semiconductor as a photocatalyst having extensive absorption in the visible region of solar light, low rate of recombination of charge carriers and stability. Among various semiconductors, TiO_2 is widely studied as a photocatalyst because of its properties such as inexpensiveness, chemical and thermal stability, low toxicity and desired conduction and valence band edge for CO_2 reduction.[12–15] However, the photocatalytic activity of TiO_2 is low in solar light, due to poor absorption in the visible region, which constitutes 43% of the solar spectrum, and a high rate of recombination of photogenerated charge carriers.[16–20] To address these issues, different strategies were adopted, such as heteroatom doping, heterojunction formation, dye sensitization, defect engineering *etc.*[21–30]

Among these, defect engineering holds promise as the presence, concentration and distribution of defects play a key role in tuning the electronic, chemical and surface properties of TiO_2. It was reported that the light absorption property of TiO_2 can be extended up to the IR region and also, the defect sites assist in adsorption and activation of the CO_2 molecule.[4] Not only the oxygen vacant site but also the uncoordinated bonds near the oxygen vacant sites help in the activation of the CO_2 molecule.[4]

There are few review articles published on the application of defective TiO_2 for CO_2 conversion.[31–34] However, they have not discussed the impact brought about by introducing defects using different synthesis methodologies on the electronic, surface and chemical properties of TiO_2 and its correlation with the photocatalytic CO_2 conversion, which is the main focus of this review article. Moreover, this article also encompasses both theoretical and experimental studies carried out on defective TiO_2 to understand the adsorption and activation of CO_2 molecules and the mechanistic insights. This review article discusses the recent development in photocatalytic CO_2 conversion using defective TiO_2. It includes the general mechanism and thermodynamic criteria for defective TiO_2 catalyzed CO_2 conversion, the theoretical investigation on the role of defects in CO_2 adsorption and activation, and the mechanism responsible for the formation and selectivity of different products. It also summarizes the effect of variation of structural and electronic properties of defective TiO_2 synthesized using various protocols on the photocatalytic conversion of CO_2 into value-added products.

Prof. Vivek Polshettiwar, after his Ph.D. in 2005, worked as a post-doc in France and the USA for a few years before starting his group at KAUST in 2009. In 2013, he moved to TIFR, and his group is working on the development of novel nanomaterials as catalysts to tackle "climate change". He has published nearly 115 articles and has an h-index of 54 and around 12700 citations in reputed journals like PNAS, Nature Comm, AngewChem, Chem. Sci., ACS Nano, ACS Catalysis, etc. He is the recipient of the prestigious ORISE Research Fellowship at the US-EPA. He was awarded Top-25 cited author in 2011 by Tetrahedron and Young Scientist Award at DSL-2012. He also received an Asian Rising Star lectureship at the 15th Asian Chemical Congress (ACC), Singapore (2013), from Nobel Laureate Professor Ei-ichi Negishi. In 2015, he was admitted as a Fellow of the Royal Society of Chemistry (RSC), United Kingdom. He was awarded the Bronze medal by the Chemical Research Society of India (CRSI), India. He was also recognized in emerging investigator-materials science and 175 faces of chemistry by the RSC, UK. He was awarded the prestigious Materials Research Society of India - MRSI Medal 2019 and Fellow Maharashtra Academy of Sciences. In 2020, he received Young Research Awards in Nano Science & Technology by DST, Gov. of India. In Jan. 2021, Vivek was elected as Fellow of the National Academy of Sciences (NASI), India.

2. General mechanism and thermodynamic criteria for photocatalytic CO_2 conversion

The photocatalytic CO_2 conversion process using semiconductor-based catalysts involves the following steps: (1) CO_2 adsorption on the surface of the catalyst, (2) generation of

electron and hole pairs after the absorption of light, (3) separation and transfer of charges to the surface active sites, and the generated charges may recombine back in the (4) bulk or (5) on the surface, (6) reduction of the adsorbed CO_2 by accepting an electron, and (7) oxidation of water to give oxygen. The processes occurring on the semiconductor surface are given in Fig. 1. Photocatalytic CO_2 conversion is a complex process and different pathways result in different products.[4] The potential energy (E^0 V *vs.* NHE at pH 7) required to form different products such as carbon monoxide (CO), formic acid (HCOOH), formaldehyde (HCOH), methanol (CH_3OH), methane (CH_4), hydrogen (H_2) and oxygen (O_2) is given as follows:

$$CO_2 + e^- \rightarrow CO_2^{\bullet -},\ E^0 = -1.90\ V \quad (1)$$

$$CO_2 + 2H^+ + 2e^- \rightarrow HCOOH,\ E^0 = -0.61\ V \quad (2)$$

$$CO_2 + 2H^+ + 2e^- \rightarrow CO + H_2O,\ E^0 = -0.53\ V \quad (3)$$

$$CO_2 + 4H^+ + 4e^- \rightarrow HCHO + H_2O,\ E^0 = -0.48\ V \quad (4)$$

$$CO_2 + 6H^+ + 6e^- \rightarrow CH_3OH + H_2O,\ E^0 = -0.38\ V \quad (5)$$

$$CO_2 + 8H^+ + 8e^- \rightarrow CH_4 + 2H_2O,\ E^0 = -0.24\ V \quad (6)$$

$$2H^+ + 2e^- \rightarrow H_2,\ E^0 = -0.41\ V \quad (7)$$

$$2H_2O \rightarrow O_2 + 4H^+ + 4e^-,\ E^0 = +0.81\ V \quad (8)$$

The water reduction process involves two electrons, whereas the reduction of CO_2 to organic products is a multielectron process. The water reduction process can compete with the CO_2 reduction reaction, and therefore, it is essential to tailor the surface of the photocatalyst in such a way that it will preferentially reduce CO_2 rather than water. Also, the single-electron transfer to the CO_2 molecule has the highest reduction potential *i.e.* −1.9 V *vs.* NHE (at pH = 7); hence it is the rate-limiting step in most of the photocatalytic CO_2 conversion reactions.[35]

3. Defective TiO_2 as a photocatalyst

3.1 Background

In 2011, Chen *et al.*[36] reported "black TiO_2" where the light absorption of anatase TiO_2 could be enhanced until 1200 nm by introducing a shell of a disordered surface layer over the core crystalline TiO_2 nanocrystal *via* a hydrogenation process. HR-TEM images after hydrogenation showed the presence of a disordered layer and a crystalline core. The hydrogenation process was carried out at 200 °C under 20 bar pressure of H_2 gas for five days. TiO_2 synthesized by this method is referred to as black TiO_2. The black TiO_2 showed enhanced photocatalytic H_2 generation in visible light with a yield of 10 000 μmol g^{-1} h^{-1}. They attributed the enhanced photocatalytic activity to the improved light absorption of black TiO_2 until 1200 nm, having an optical bandgap of 1.54 eV. The introduction of mid-gap electronic states within the bandgap of TiO_2 was due to the presence of lattice disorder with H atom doping, which improved light absorption.

After this discovery, a range of methodologies for defect creation was adopted to improve the light absorption of TiO_2 in the visible region. Defects were generated in TiO_2 using different synthesis methodologies such as hydrogen gas treatment, inert gas treatment, plasma treatment, metallothermic reduction, using a reducing agent, bombardment with high energy particles, hydrolysis of Ti^{4+} salt in the presence of a reductant, doping with a heteroatom, *etc.*[31–34]

3.2 Role of defects in CO_2 adsorption–activation and light harvesting

The electronic, optical, surface and chemical properties of TiO_2 are dependent on the type and concentration of the defects present in it. These properties play a crucial role in determining the photocatalytic activity of the material. Defects in crystals are classified depending on the dimensionality as 0D point defects, 1D line defects, 2D planar defects and 3D bulk defects.[37] Point defects in TiO_2 include Ti vacancies, oxygen vacancies, and Ti

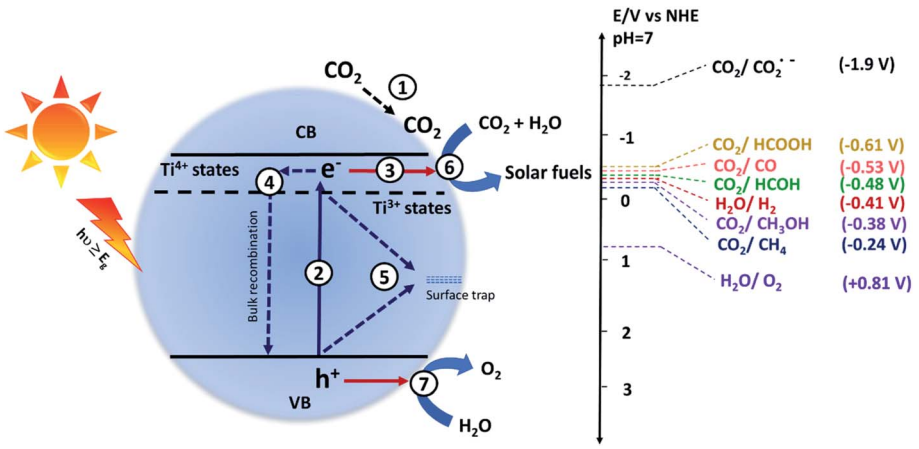

Fig. 1 Schematic illustration of different processes occurring during the photocatalytic conversion of CO_2 into useful products. The absorption of light energy equal to or greater than the bandgap (E_g) resulting in excitation of the electrons from the valence band (VB) to the conduction band (CB), leaving behind holes in the VB. The electrons and holes promote the reduction and oxidation of the reactant molecules, respectively.

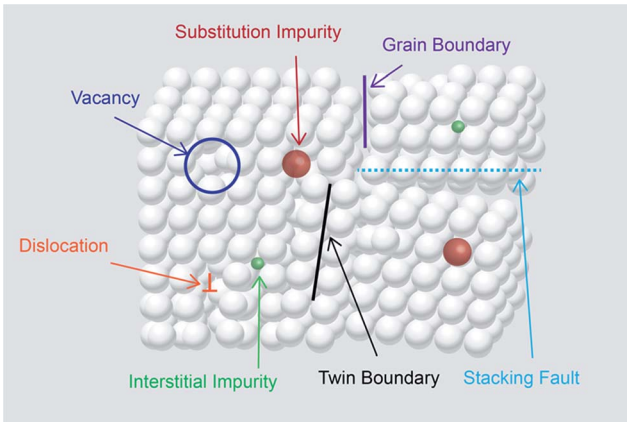

Fig. 2 Schematic of the different types of defects present in the TiO_2 crystal.

interstitial and substitutional or interstitial impurity.[37,38] Line defects are described as extended dislocations.[39] 2D defects (planar defects) contain grain boundaries, twin boundaries and stacking faults. Bulk defects (volume defects) include inclusions, cracks, voids and pores.[37] Fig. 2 shows the types of defects present in the crystal.

The generation of oxygen vacancies is the easiest as compared to the generation of interstitial vacancies.[40] Oxygen removal leaves behind two electrons at the vacant oxygen site. These electrons were accepted by the adjacent Ti^{4+} present near the oxygen vacant site to generate Ti^{3+} sites.[41] The preliminary step in CO_2 conversion is the adsorption of CO_2 molecules on the catalyst surface. The presence of oxygen defects not only facilitates the reduction of the bandgap of pristine TiO_2 but also generates active sites for CO_2 adsorption and activation, thus making it a suitable candidate for photocatalytic CO_2 conversion using solar energy. Several theoretical studies have been performed to understand the role of defects in CO_2 activation and conversion into different products.

Oxygen vacant sites offer a stronger binding site for CO_2 adsorption. Thompson *et al.*[42] studied the adsorption and desorption of CO_2 on the oxidized and defective TiO_2 (110) surfaces by temperature-programmed desorption. In the case of a fully oxidized surface, CO_2 binds to the fivefold coordinated Ti^{4+} atoms, whereas in the case of the defective TiO_2 surface, CO_2 binds to both the regular sites and to the oxygen vacant sites. They also found that the CO_2 binds to the oxygen vacant sites with a higher binding energy of 54 kJ mol^{-1} than the regular sites (48.5 kJ mol^{-1}).

Huygh *et al.*[43] studied the adsorption, dissociation and diffusion of CO_2 on the oxidized and reduced (001) surfaces of anatase TiO_2 using density functional theory (DFT) calculations with long-range dispersion energy corrections. Fig. 3a shows the different vacancy sites present on the (001) anatase surface, namely V_{O1}, V_{O2}, V_{O3} and V_{O4}. They identified the monodentate carbonate structure as the stable adsorption configuration after the interaction of CO_2 with the oxidized surface. A small energy barrier exists for the conversion of physisorbed CO_2 to a chemisorbed one. CO_2 dissociation is not possible on an oxidized surface because of having a barrier of 113.6 kcal mol^{-1}. However, the presence of an oxygen vacancy provides a new, highly stable adsorption configuration of CO_2 with the elongation of the C–O bond (Fig. 3b). The activation of the C–O bond results in exothermic dissociation of CO_2 with a barrier of 22.2 kcal mol^{-1}. The CO_2 dissociation on the vacant oxygen site has a lower barrier than on the oxidized surface as the former provides a way to stabilize the end product by taking up the oxygen from CO_2 to fill the vacant oxygen site. This results in the formation of a CO molecule, which is desorbed by filling the vacant site.

Lee *et al.*[44] studied the electron-induced dissociation of CO_2 adsorbed at the oxygen vacant site on the TiO_2 (110) surface by scanning transmission microscopy (STM). Fig. 4a shows the schematic of the TiO_2 (110) surface having the oxygen vacancy (V_O), bridged hydroxyl group (OH_b) and CO_2 adsorbed at the vacant site. The inset shows the tilted configuration of CO_2 adsorbed at the vacant oxygen site. They found that the most stable adsorption of CO_2 at the vacant site was a nearly linear configuration with an adsorption energy of 0.44 eV. Fig. 4b shows the STM images recorded after exposure to CO_2 at 55 K. The inset shows the STM images of the same area before and after CO_2 thermal diffusion. They observed that the two CO_2 molecules shown in the dotted ellipse in the upper inset diffused away from their V_O site, leaving behind two intact V_O sites as seen in the dotted ellipse of the lower inset. This revealed that the CO_2 was adsorbed at the V_O site. Fig. 4c shows

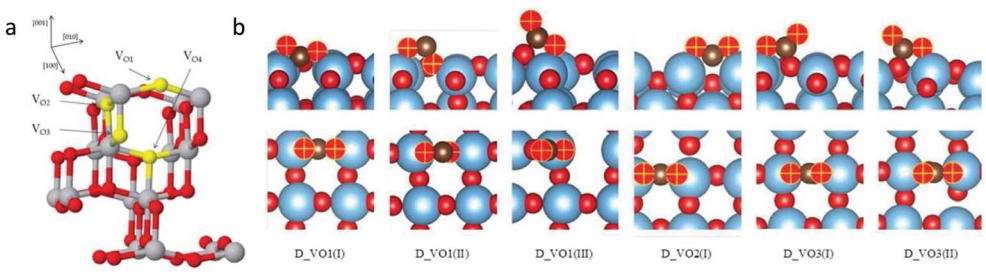

Fig. 3 (a) Type of oxygen vacancies on the (001) surface of anatase TiO_2 (Ti = gray, O = red, oxygen vacancy = yellow) and (b) adsorption configurations of CO_2 on the reduced TiO_2 anatase surface with different vacancies in side view (upper panel) and top view (lower panel) (Ti = blue, O_{TiO_2} = red, O_{CO_2} = red and yellow plus sign and C = brown) (reproduced from ref. 43 with permission from the American Chemical Society, copyright 2016).

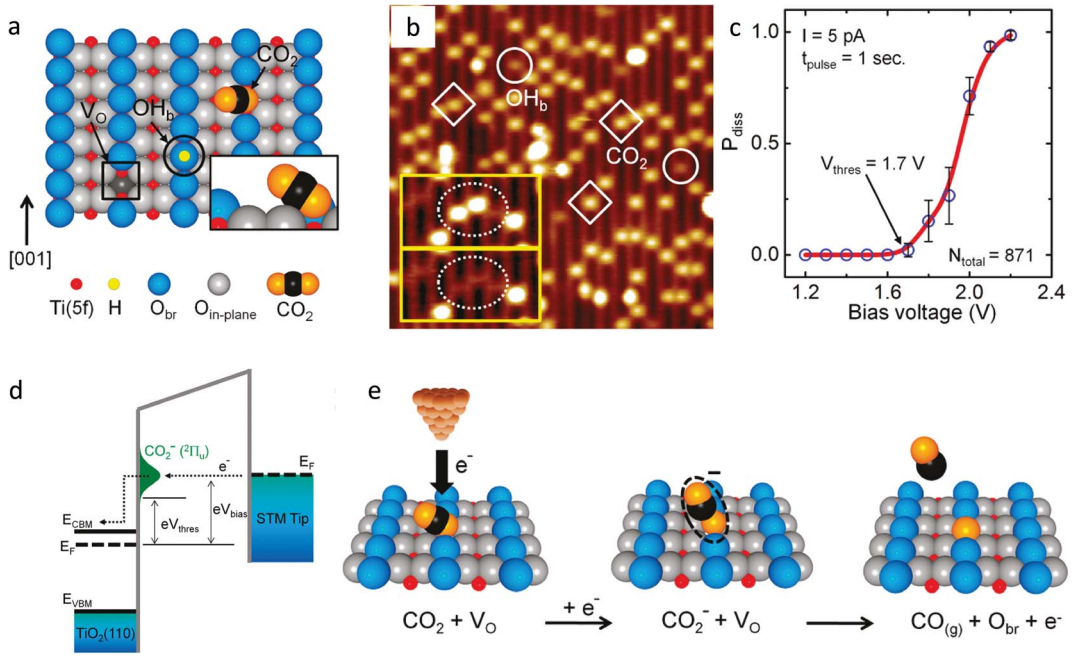

Fig. 4 (a) Schematic showing the oxygen vacancy (V_O, in a black color square), bridged hydroxyl group (OH_b, black color circle) and CO_2 molecule adsorbed at the V_O site on the reduced TiO_2 (1) (1 × 1) surface. The fivefold-coordinated Ti(5f) atoms and bridged oxygen (O_{br}) are indicated in red and blue, respectively. The inset shows that the molecular axis of CO_2 is perpendicular to the direction of the bridging-oxygen row ([001] azimuth) and is tilted away from the surface normal by 57°; (b) STM image (1.5 V, 5 pA, 15 nm × 15 nm) of the TiO_2 (110) surface after adsorption of CO_2 at 55 K. Three CO_2 and two OH_b features are shown as diamonds and circles, respectively. The inset shows two STM images (5.1 nm × 2.6 nm) of the same area on the surface. The upper inset shows two CO_2 molecules (in the dotted ellipse) that diffused away from their V_O sites, leaving two intact V_O sites visible, as shown in the lower inset image; (c) dissociation probability (P_{diss}) plotted as a function of bias voltage. The threshold voltage was V_{thres} = +1.7 V, and P_{diss} approached 1 at +2.2 V. (d) The electron-transfer process at the STM tip/CO_2/TiO_2 interface. Above eV_{thres} = 1.7 eV, the electrons start to tunnel into the negative-ion state of the adsorbed CO_2 and (e) schematics of an electron-induced CO_2 dissociation process (reproduced from ref. 44 with permission from the American Chemical Society, copyright 2011).

that 1.7 V is the threshold energy required for the dissociation of CO_2 and the probability of dissociation depends on the energy of the injected electron from STM tip.

The electron from the Fermi level of STM tip can tunnel into CO_2 to form CO_2^- in the $^2\Pi_u$ state if the energy of the electron is greater than 1.7 eV (Fig. 4d). As the Fermi level lies 0.3 eV below the CB, the threshold energy is located 1.4 eV above the CB. They demonstrated that the dissociation of CO_2 is a one-electron process with a threshold energy of 1.4 eV above the conduction band minimum of TiO_2. The CO_2 adsorbed at the oxygen vacant sites dissociates by accepting an electron and heals the vacancy by the oxygen released during dissociation reaction (Fig. 4e). The CO molecule formed could be desorbed from the surface by the excess energy gained during the dissociation process. The formation of CO_2^- species is the key intermediate in CO_2 dissociation. Similar results were also reported by Tan *et al.*[45] where they studied the activation of CO_2 on the rutile TiO_2 (110) (1 × 1) surface by injecting an electron to CO_2 by *in situ* STM at 80 K.

The presence of point defects creates energy levels within the bandgap and hence light absorption by TiO_2 can extend up to the near IR region. Hossain *et al.*[46] used *Ab initio* density functional theory to calculate the formation energy of intrinsic point defects and position of the defect-induced energy levels within the bandgap of reduced rutile TiO_{2-x}. They reported the energy levels for the oxygen vacancy (V_O), titanium vacancy (V_{Ti}) and titanium interstitial (Ti_{int}) as 1.17, 1.15 and 1.23 eV, respectively (Fig. 5). The presence of these defects can be thoroughly analyzed by the scanning transmission microscopy (STM) in combination with density functional theory (DFT), high-resolution transmission electron microscopy (HR-TEM), positron annihilation spectroscopy (PAS), electron paramagnetic resonance (EPR), magnetism testing, temperature-programmed desorption (TPD), Fourier transform infrared spectroscopy (FTIR), optical absorption spectroscopy, X-ray photoelectron spectroscopy (XPS), and Raman spectroscopy.[31–34]

3.2 Mechanistic pathways for photocatalytic CO_2 conversion using defective TiO_2

Two pathways were proposed based on the adsorption and the binding of CO_2 to the catalyst surface. One is the carbene pathway and the other is the formaldehyde pathway.[47] In the carbene pathway, the $CO_2^{\bullet-}$ radical is formed by accepting an electron from the TiO_2 catalyst. $CO_2^{\bullet-}$ binds in a bidentate mode to the two Ti atoms on the surface *via* a carbon atom. These radicals undergo reduction by accepting hydrogen radicals and electrons to form CO. The adsorbed CO on further reduction in multiple steps gives a $^{\bullet}$CH radical, carbene, and a methyl radical as intermediates to finally give methanol or methane as the final product.

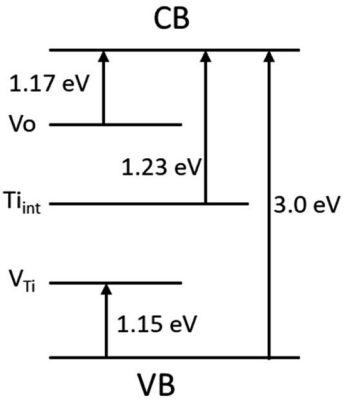

Fig. 5 Energy levels formed due to the presence of defects such as oxygen vacancy, titanium vacancy and titanium interstitial within the bandgap of reduced rutile TiO_{2-x}. Energy levels were taken from ref. 46.

In the formaldehyde pathway, the carboxy radical ($^{\bullet}$COOH) is primarily formed as a result of binding of the CO_2 molecule in a monodentate mode either through binding of the oxygen atom of CO_2 to Ti or binding of the oxygen atom of the surface to the carbon atom of the CO_2. The $^{\bullet}$COOH forms formic acid by accepting hydrogen radicals. On further reduction of formic acid, formaldehyde, methanol and methane is produced through a series of electron transfer and dehydrating steps.

To understand the mechanism of CO_2 reduction on the perfect and defective (101) surfaces of anatase TiO_2, Ji *et al.*[48] carried out first principles calculation. They concluded that in the case of both defective and non-defective TiO_2, the fast hydrogenation (FH) pathway, generally known as the formaldehyde pathway, is most preferred over the fast deoxygenation (FDO) pathway (known as the carbene pathway). FDO is not possible due to the formation of the energetically unfavorable $^{\bullet}$C intermediate. They also found that the surface oxygen vacancies are more active than Ti atoms on the surface. A new mechanism was proposed to explain the selectivity of the reaction in which fast hydrogenation occurs at both Ti as well as oxygen vacancies and is shown in Fig. 6. On the V_O site, the deoxygenation of CO_2 is easier and the two electrons provided by the defect sites could prevent the photooxidation of the intermediate species and promote their further reduction.

To further understand the mechanism proposed by Ji *et al.*,[48] Liu *et al.*[49] performed a DFT calculation to study the pathway for methane and methanol formation from CO_2 reduction over the defective anatase phase of TiO_2 with the (101) surface. They found that the reaction proceeds through the two plausible pathways (Fig. 7) as follows $CO_2 \rightarrow CO(A)(CO(B)) \rightarrow CHO(CHO) \rightarrow CHOH(CH_2O) \rightarrow CH_2OH(CH_3O) \rightarrow CH_3OH^*$ or CH_4. CO(A) and CO(B) stand for a more stable monodentate configuration with C binding to Ti^{3+} and a less stable bidentate configuration of CO on the V_O site of the surface, respectively. The desorption energy of methanol is high as 1.66 eV, indicating that it will be difficult to desorb from the V_O site of the surface and thus stable on the surface at room temperature. The barrier for the conversion of adsorbed methanol to CH_3 is very low *i.e.*, 0.18 eV, and thus, the formation of CH_3 is more favorable than the desorption of the adsorbed methanol. Methane is expected as the reaction product as the desorption energy of methane is only 0.20 eV. The predicted mechanism matches with the experimental findings as CO and CH_4 were the experimentally observed products.

Furthermore, they also considered a carbene-like deoxygenation pathway to form the CH species on the vacant site, which could generate methane by successive hydrogenation steps.[49] The proposed direct deoxygenation and hydrogenation pathway is $CO_2 \rightarrow CO(A) \rightarrow CHO \rightarrow CHOH \rightarrow CH \rightarrow CH_2 \rightarrow CH_3 \rightarrow CH_4$. The rate-limiting step in this pathway is CHOH → CH with a barrier of 1.96 eV, which is much lower than that reported by Ji *et al.*[48] All the pathways from CO_2 are thermodynamically feasible but the barriers between the steps are high mainly in the carbene pathway. The energy *via* electric field or electrochemical potential could be used to increase the rate of the reaction and, thus, product yield. From the theoretical study, it was concluded that the formaldehyde pathway is more preferred over the carbene pathway for CO_2 conversion in defective TiO_2. Methane formation is preferred over methanol due to its high desorption energy.

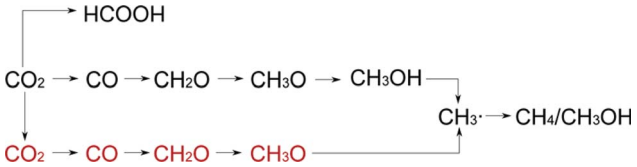

Fig. 6 Reaction pathway for the photocatalytic CO_2 conversion (red and black color font indicate the species adsorbed at the oxygen vacancy and on surface Ti, respectively) (reproduced from ref. 48 with permission from the American Chemical Society, copyright 2016).

4. Defect generation in TiO_2 and its impact on photocatalytic CO_2 conversion

The various synthesis procedures, the physicochemical changes in TiO_2 due to the presence of defects and applications of defective TiO_2 for photocatalytic CO_2 conversion are summarized in this section. Point defects in TiO_2 can be introduced by different ways, such as reduction using hydrogen gas, inert gas treatment, a reducing agent like $NaBH_4$, metallothermic reduction by using metals like Al, Mg, Li, Zn, *etc*, bombardment with high energy particle such as electron beam, proton beam, hydrogen plasma, electrochemical reduction method, doping with a heteroatom, *etc.* The details of the synthesis methodologies have been given in more detail in several other articles.[31–34,37] This review primarily focuses on the defects generated using different synthesis methodologies and their impact on the physicochemical and photocatalytic properties of TiO_2.

4.1 Defect generation under a reducing atmosphere

4.1.1 Hydrogen atmosphere. In this method, defects were generated under a hydrogen atmosphere. Pure H_2 gas or a mixture of H_2/Ar or H_2/N_2 gases and also the hydrides (such as $NaBH_4$ and CaH_2), which releases active hydrogen species, were

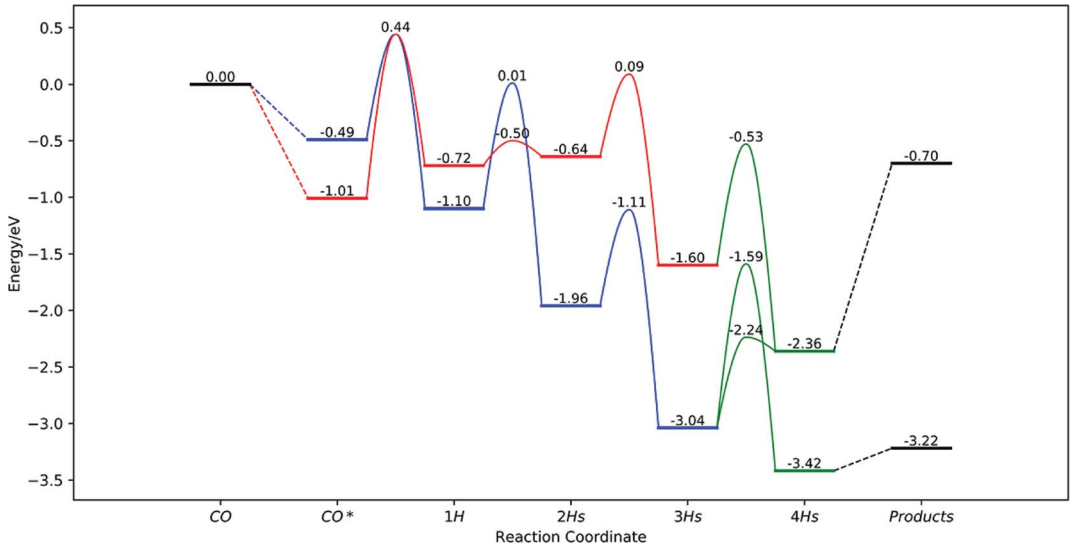

Fig. 7 Overall potential energy surface from CO to CH_4. Black, red, blue, and green bars and curves represent a desorption state, the most favorable pathway for CO(A), the most favorable pathway for CO(B) and pathways after merged, respectively (reproduced from ref. 49 with permission from the American Chemical Society, copyright 2019).

used as the hydrogen source.[50] The application of hydrogen treated defective TiO_2 was reported for CO_2 conversion by different research groups.

The general representation of the TiO_2 reduction reaction in the presence of hydrogen gas can be given by the below equation. The hydrogen reacts with the lattice oxygen of TiO_2 to form oxygen vacancies and Ti^{3+} in TiO_2.

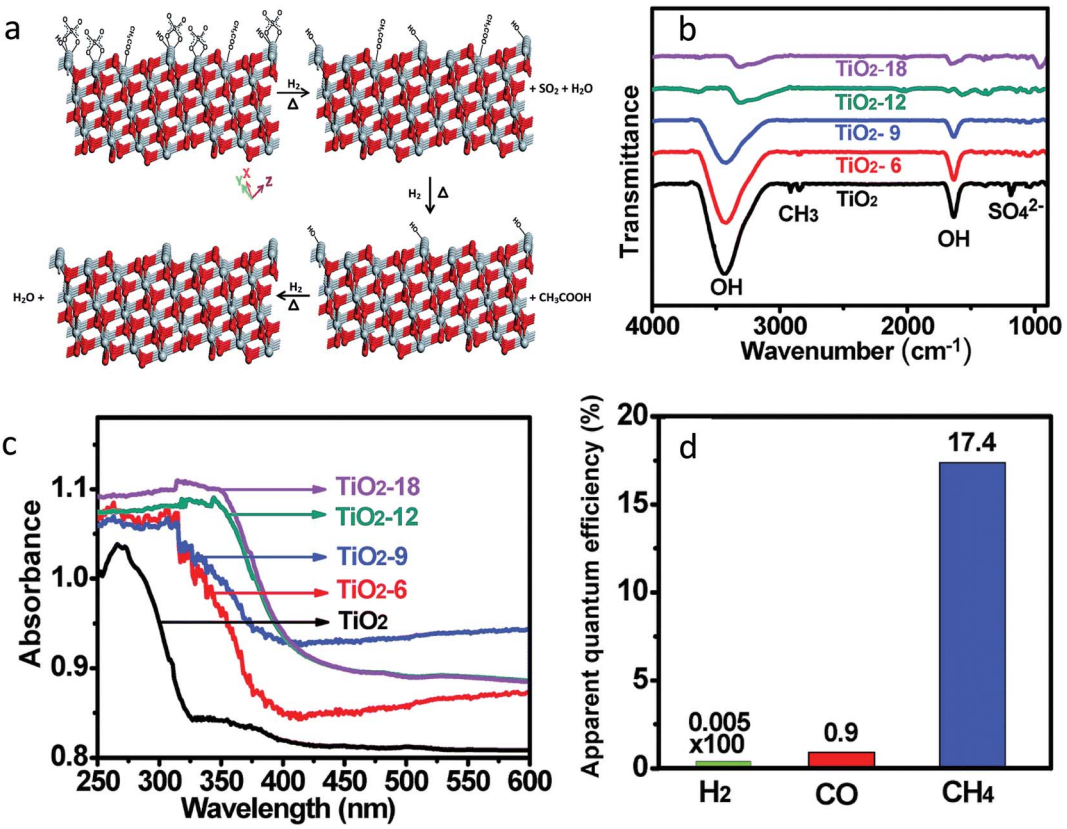

Fig. 8 (a) Schematic of the chemical reaction that occurred on the surface of the TiO_2 during hydrogenation (gray color: Ti and red color: O), (b) FTIR spectra of non-hydrogenated and hydrogenated TiO_2 samples, (c) diffuse reflectance spectra of TiO_2 and hydrogenated samples and (d) apparent quantum efficiency (AQE) for H_2, CO and CH_4 using the TiO_2-12 sample (reproduced from ref. 51 with permission from the Royal Society of Chemistry, copyright 2019).

$$TiO_2 + H_2 \rightarrow TiO_{2-x} + H_2O \quad (9)$$

The chemical properties of TiO_2 nanomaterials are greatly affected by their size, morphology, shape, exposed facets on the surface and the concentration of defects.[31] These factors make hydrogen thermal treatment more complicated. The experimental parameters such as the amount of TiO_2, pressure and concentration of the hydrogen and reaction temperature and time affect the chemical, optical and electronic properties as well as the concentration of defects in the hydrogenated TiO_2. Hydrogenation helps in the generation of the Ti^{3+} sites as well as cleaning the surface of the photocatalyst. Recently, Liu *et al.*[51] synthesized TiO_2 nanotubes/nanowires with exposed {111} facets by heating a mixture of titanium(IV) oxysulfate–sulfuric acid hydrate, glacial acetic acid and water. These as-synthesized TiO_2 nanotubes/nanowires were hydrogenated at 650 °C under H_2 gas flow of 2.0 L h^{-1} for 6, 9, 12 and 18 h and referred to as TiO_2-6, TiO_2-9, TiO_2-12 and TiO_2-18, respectively. No change in morphology after hydrogenation was observed. The hydrogenation process causes the expansion and distortion of the TiO_2 crystal lattice as revealed from the XRD pattern. The chemical reactions that occurred on the surface during hydrogenation are shown in the schematic in Fig. 8a. The absorption band corresponds to SO_4^{2-} and CH_3COO^- species which accumulated in the course of synthesis and disappeared completely after 6 h of hydrogenation (Fig. 8b). During the hydrogenation process, these species get removed and the surface becomes clean. The amount of Ti^{3+} increases with an increase in the hydrogenation time, as revealed from the XPS spectra. Fig. 8c shows that the light absorption enhanced in the visible region with the increase in the duration of hydrogenation. The bandgap value varies from 3.40 eV for TiO_2 to 2.64 eV for TiO_2-18.

Photocatalytic CO_2 conversion was carried out in the presence of isopropanol as a sacrificial reagent at 0.2 MPa of CO_2 and 373 K temperature. The photocatalytic CO_2 reduction activity increases in the order P25 < TiO_2 < TiO_2-6 < TiO_2-9 < TiO_2-12 < TiO_2-18, indicating that the activity of TiO_2 nanostructures could be increased by hydrogenation. H_2, CO and CH_4 were generated at a rate of 2.11, 463.2 and 1708.08 μmol g^{-1} h^{-1} using TiO_2-12, respectively. 17.4% apparent quantum efficiency (AQE) for methane generation was observed using a hydrogenated TiO_2-12 sample (Table 1, Fig. 8d). The improved activity was attributed to the exposed clean {111} facets and enhanced light absorption. The author proposed a mechanism where photogenerated electrons and holes transferred to TiO_2 (111) and $(\bar{1}\bar{1}\bar{1})$ surfaces due to the generated spontaneous electric field between the two polar planes, respectively. Thus, the redox reaction takes place at two different Ti–TiO_2 (111) and O–TiO_2 $(\bar{1}\bar{1}\bar{1})$ polar planes. This resulted in a better separation of charge carriers and improved photocatalytic activity.

Furthermore, the effect of particle size on the degree of hydrogenation and its impact on photocatalytic CO_2 conversion was studied by Xuan *et al.*[52] In this work, the TiO_2 nanoparticles were loaded over dendritic porous silica nanospheres (DPSNs), also known as dendritic fibrous nanosilica (DFNS). The particle size of TiO_2 was tuned from 1–2 to 9–12 nm by varying the amount of titanium isopropoxide precursor. To create oxygen vacancies, hydrogen thermal reduction treatment at ambient pressure was carried out by flowing a mixture of gas containing 5 vol% H_2 and 95 vol% argon at 600 °C for 3 h. The synthesis methodology is given in Fig. 9a. Samples were referred to as DPSNs@*X*% TiO_{2-x} where *x* is the weight ratio of TiO_2/DPSNs. The only signal that corresponded to the oxygen vacancy was observed in the EPR spectrum. The sample DPSNs@*X*% TiO_{2-x} (*X*% ≤ 20%) having a particle size of 1–3 nm of TiO_{2-x} nanoparticles (NPs) showed CO as the only product of CO_2 conversion, whereas 3–12 nm TiO_{2-x} NPs on DPSNs@*X*% TiO_{2-x} (*X*% ≥ 40%) showed the generation of both the CO and CH_4 (Fig. 9b). The maximum CH_4 and CO generation at a rate of 124.3 and 14.7 μmol g^{-1} of TiO_{2-x} h^{-1} was observed using DPSNs@80% TiO_{2-x} having a particle size of 8–12 nm of TiO_{2-x}, respectively. They found that 1–3 nm TiO_{2-x} nanoparticles showed a higher reduction degree during hydrogen thermal treatment leading to a higher decrease in the bandgap. This could have resulted in the lowering of the reduction power of the electrons, which inhibited the kinetics of the reduction reaction of CO_2 to methane involving eight electrons (Fig. 9c and d). The exact reason for the improved selectivity of 89.4% for methane production in DPSNs@80% TiO_{2-x} was unclear and they attributed it to the improved light absorption efficiency and suitable CB edge, which help maintain the reduction ability of photogenerated electrons. The other factors such as the better dispersion of particles, appropriate particle size, highly accessible specific surface area, the lower recombination rate of photogenerated charge carriers, and enhanced carrier transfer and separation also contributed to the improvement of the photocatalytic CO_2 conversion yield in DPSNs@80% TiO_{2-x}.

Hydrogenation using H_2 atmosphere was also beneficial to reduce metal ions into metals along with the generation of oxygen vacancies and Ti^{3+} in TiO_2. Billo *et al.*[53] introduced dual active sites, Ni nanocluster and the oxygen vacancies for the enhanced CO_2 conversion. For this, Ni nanocluster supported oxygen-deficient black TiO_2 was synthesized *via* the one-pot hydrothermal process, followed by hydrogenation under pure H_2 gas flow at 300 °C for 3 h. The sample before and after hydrogenation was referred to as Ni/TiO_2 and Ni/TiO_2[V_O], respectively. The hydrogenation treatment brings about the instantaneous reduction of NiO to Ni nanoclusters on black TiO_2. The lattice disorder and Ni nanoclusters on the hydrogenated TiO_2 surface resulted in the formation of mid-gap states and enhanced light-harvesting capability in Ni/TiO_2[V_O], as shown in Fig. 10a. The Ni/TiO_2[V_O] catalyst showed an acetaldehyde yield of 10 μmol g_{cat}^{-1} in 6 h with 100% selectivity, which was 2 and 18 times higher than that of Ni/TiO_2 and commercial TiO_2 (P25) under (300 W) halogen lamp illumination, respectively (Fig. 10b). The reaction mechanism for improved selectivity was not clear. The band edge position was derived from ultraviolet photoelectron spectroscopy (UPS) and DRS absorption data. From this data, they concluded that the improved selectivity for acetaldehyde in Ni/TiO_2[V_O] could be because of the higher CB position at −1.3 V *vs.* NHE than the Ni/TiO_2 (−1.16 V *vs.* NHE) (Fig. 10c). The proposed mechanism for CO_2 conversion is shown in Fig. 10d. The work function of Ni metal (5 eV) was higher than that of the Ni/TiO_2[V_O] (3.75 eV),

Table 1 Photocatalytic CO_2 conversion using defective TiO_2

Sr no.	Reference	Chemicals used to create defects	Photocatalytic experimental conditions	Light source used	Products	Yield	AQE/SFE
1	Liu *et al.*[51]	H_2 gas	10 mg catalyst dispersed in 1.0 mL $(CH_3)_2CHOH$ and 4.0 mL H_2O, (0.2 MPa) CO_2	300 W Xe lamp	CH_4	1708.1 μmol g^{-1} h^{-1}	AQE: 17.40%
					CO	463.2 μmol g^{-1} h^{-1}	—
					H_2	2.11 μmol g^{-1} h^{-1}	—
2	Xuan *et al.*[52]	H_2 gas	25 mg of catalyst, CO_2 was generated inside the reactor	300 W Xe lamp, intensity on the sample was 0.5W cm^{-2}	CH_4	124.3 μmol g^{-1} h^{-1}	—
					CO	14.7 μmol g^{-1} h^{-1}	—
3	Billo *et al.*[53]	H_2 gas	CO_2 bubbled through water, co-catalyst: Ni	300 W Xe lamp	CH_3CHO	10 μmol g^{-1} in 6 h	—
4	Fu *et al.*[54]	H_2 gas	100 mg of catalyst, CO_2 bubbled through water	Solar simulator AM 1.5	CH_3CHO	11.3 μmol g^{-1} in 6 h	—
					CH_3OH	1.2 μmol g^{-1} in 6 h	—
5	Ye *et al.*[55]	H_2 gas	Sample concentration 1 g L^{-1}, CO_2 flow rate 100 mL min^{-1}, NaOH = 0.20 mol L^{-1}, Na_2SO_3 = 0.20 mol L^{-1}, reaction temperature 5 °C	300 W Xe lamp	CO	12.1 μmol g^{-1} h^{-1}	—
6	Liu *et al.*[56]	H_2 gas	50 mg catalyst, CO_2 passed through water	150 W solar simulator (90 mW cm^{-2})	CH_4	4.4 μmol g^{-1} in 6.5 h	—
					CO	25 μmol g^{-1} in 6.5 h	—
7	Li *et al.*[57]	N_2 : H_2(9 : 1)	50 mg catalyst dispersed in 2 mL of water, CO_2 gas passed through it temperature: 393 K, co-catalyst: CoO_x	150 W UV lamp (20 mW cm^{-2} at 365 nm)	CH_4 (selectivity: 71.02%)	10.1 μmol g^{-1} h^{-1}	0.0126
					CO (selectivity: 28.98%)	16.4 μmol g^{-1} h^{-1}	—
8	Sorcar *et al.*[59]	$NaBH_4$	40 mg of catalyst, moist CO_2 (40 mL min^{-1}), co-catalyst: Pt (0.33 wt%)	100 W Xe solar simulator (AM1.5 filter)	CH_4	80.3 μmol g^{-1} h^{-1}	12.4
9	Sorcar *et al.*[60]	$NaBH_4$	40 mg of catalyst, moist CO_2 (40 mL min^{-1}), co-catalyst: Pt 1 wt%	100 W Xe solar simulator (AM1.5 filter)	C_2H_6	77 μmol g^{-1} in 7 h	2.7
					CH_4	259 μmol g^{-1} in 7 h	5.2
10	Sorcar *et al.*[61]	$NaBH_4$	40 mg of catalyst, moist CO_2 (40 mL min^{-1}), co-catalyst: Cu–Pt	100 W Xe solar simulator AM1.5 filter	C_2H_6	150 μmol g^{-1} in 6 h	Total AQE: 86%, SFE: 1%
					CH_4	3000 μmol g^{-1} in 6 h	—
11	Yan *et al.*[62]	H_2 plasma	90 mg photocatalyst, CO_2 bubbled through water	550 W Xe-lamp with an AM 1.5 G filter, 100 mW cm^{-2}	CH_4	14.03 nmol h^{-1} in 90 mg	—
					CO	21.67 nmol h^{-1} in 90 mg	—
12	Liu *et al.*[63]	He gas	100 mg catalyst, CO_2 and H_2O vapor ($H_2O \approx$ 2.3 v/v%),	150 W solar simulator, AM1.5 filter; 90 mW cm^{-2}	CH_4 + CO	18.9 μmol g^{-1} in 6 h	—
13	Xin *et al.*[64]	Oxidation-based hydrothermal method	Flow reactor (2 mL min^{-1}) CO_2 bubbled through water	300 W Xe lamp, vis-light, 0.216W cm^{-2} (≥420 nm)	CH_4	11.9 μmol g^{-1} h^{-1}	—
					CO	23.5 μmol g^{-1} h^{-1}	—
14	Zhao *et al.*[65]	Vacuum annealing	20 mg catalyst dispersed over a quartz disc with a diameter of 50 cm^2, CO_2 from $NaHCO_3$ and H_2SO_4	500 W Xe lamp, 0.220 W cm^{-2}, (400–800 nm)	CO	48.5 μmol g^{-1} in 6 h	—
					CH_4	8 μmol g^{-1} in 6 h	—
15	Kar *et al.*[66]	Flame reduction method	TiO_2 nanotube array with an area of 1 cm × 2 cm, 50 psi CO_2 pressure and 80 °C to vaporize the water, a few droplets of water were placed in the reactor beside the catalyst without direct contact with the catalyst	300 W Xe lamp AM1.5 filter	CH_4	156.5 μmol g^{-1} h^{-1}	—

Table 1 (*Contd.*)

Sr no.	Reference	Chemicals used to create defects	Photocatalytic experimental conditions	Light source used	Products	Yield	AQE/SFE
16	Tu *et al.*[67]	*In situ* simultaneous reduction–hydrolysis technique	100 mg photocatalyst, CO_2 at ambient pressure, 0.4 mL H_2O	300 W Xe lamp	CH_4 C_2H_6	8 μmol g^{-1} h^{-1} 16.8 μmol g^{-1} h^{-1}	— —
17	Yin *et al.*[69]	Aluminothermic reduction	50 mg catalyst, 2 bar CO_2, 6 mL H_2O	300 W Xe lamp	CH_4 (selectivity: 74%)	14.3 μmol g^{-1} h^{-1}	—
18	Gao *et al.*[70]	Aluminothermic reduction	Two pieces of the black TiO_2 NTAs catalyst – equivalent to 0.01 g TiO_2, CO_2 is introduced in solution	300 W Xe lamp with a 420 nm cut-off filter	CO	185.39 μmol g^{-1} h^{-1}	—
19	Wang *et al.*[72]	Lithiothermic reduction	100 mg photocatalyst, 0.4 mL water, CO_2, co-catalyst: 1 wt% Pt	300 W xenon arc lamp equipped with a UV light filter (~100 mW cm^{-2})	CH_4 (visible light) CH_4 (UV-visible light)	3.37 μmol g^{-1} in 8 h 8.85 μmol g^{-1} in 8 h	— —
20	Sasan *et al.*[73]	One-step combustion and hydrothermal methods	100 mg catalyst held on a Teflon holder, 4 mL liquid water at the bottom of reactor, CO_2, co-catalyst: Cu(I)–Pd (1 wt%)	Xe lamp (300 W) with 400 nm cut-on filter	CH_4	~6 μmol g^{-1} in 6 h	—
21	Fang *et al.*[74]	Hydrothermal method using HCl and a small amount of HF	0.03 g of catalyst amount, 1 mL pure water, batch reactor, no co-catalyst	300 W Xe lamp AM1.5 filter	CH_4 CO	~0.9 μmol g^{-1} in 4 h ~0.8 μmol g^{-1} in 4 h	— —
22	Liu *et al.*[75]	$NaBH_4$ reduction	40 mg catalyst spread over a glass fiber filter, CO_2 bubbled through water, temperature: 150 °C, no cocatalyst	100 W Hg vapor lamp with 10 mW cm^{-2} at λ < 390 nm 300 W Xe lamp with UV filter 28 mW cm^{-2} in visible range	CO (UV-visible) (Visible)	54.5 μmol g^{-1} in 5 h 26.5 μmol g^{-1} in 5 h	0.31 0.134
23	Liu *et al.*[76]	Ultrathin nanosheets of TiO_2 by hydrothermal synthesis	10 mg of sample spread in a chamber, CO_2 passed through water (0.08 MPa), co-catalyst: Pt	300 W xenon lamp	CH_4 CO	66.4 μmol g^{-1} h^{-1} 54.2 μmol g^{-1} h^{-1}	— —
24	Shi *et al.*[77]	Solvothermal method using HF	50 mg sample, CO_2 bubbled through water, H_2O/CO_2 = 2.3v/v%	100 W mercury lamp (λ = 365 ± 10 nm)	CH_4	2.49 μmol g^{-1} h^{-1}	—
25	Qingli *et al.*[78]	Treatment of the Ti plate in H_2O_2 solution at 110 and 130 °C (hydrothermal treatment)	TiO_2 film, CO_2 bubbled through water	Two 300 W Xe lamps	CH_4 CO	12 μmol g^{-1} h^{-1} 115 μmol g^{-1} h^{-1}	— —
26	Liu *et al.*[79]	Fluoride mediated self-transformation pathway	30 mg of photocatalyst, Na_2CO_3 + H_2SO_4, batch reactor, cocatalyst: Au	300 W Xe lamp	CO CH_4	~2.1 μmol g^{-1} h^{-1} ~1.2 μmol g^{-1} h^{-1}	— —
27	Yin *et al.*[80]	Solvothermal method with Li-dissolved EDA as solution. (Considerable number of defects (V_O or Ti^{3+}) existed in H–TiO_{2-x})	50 mg catalyst, 2 bar CO_2, 6 mL H_2O	300 W Xe lamp, simulated solar AM1.5 filter	CH_4 CO H_2	16.2 μmol g^{-1} h^{-1} 4.2 μmol g^{-1} h^{-1} 13 μmol g^{-1} h^{-1}	— — —

Table 1 (*Contd.*)

Sr no.	Reference	Chemicals used to create defects	Photocatalytic experimental conditions	Light source used	Products	Yield	AQE/SFE
28	Zhu *et al.*[81]	*In situ* photodeposition of Cu generates *in situ* oxygen vacancies	30 mg catalyst,6 μL of water	300 W commercial Xe lamp	CH_4	8.68 μmol g^{-1} h^{-1}	—
29	Lan *et al.*[82]	No such defect is created. Doping of Cu metal by the solvothermal method induced oxygen vacancies	30 mg of catalyst, CO_2 bubbled through solution	300 W Xe lamp	CO	32.5 μmol g^{-1} h^{-1}	—
30	Pham *et al.*[83]	Codoping of Ag and Cu into the TiO_2 lattice	2 g of catalyst CO_2 passed through water was injected inside the reactor	Visible light. (Two 20 W bulbs of 0.05 W cm^{-2})	CO CH_4	550 μmol g^{-1} in 6 h 880 μmol g^{-1} in 6 h	— —
31	Pham *et al.*[84]	Co-doping of V and Cu into TiO_2 lattice	2 g of catalyst CO_2 was injected inside the reactor	Visible light. (Two 20 W bulbs of 0.05 W cm^{-2})	CH_4 CO	933 μmol g^{-1} in 6 h 588 μmol g^{-1} in 6 h	— —
32	Wang *et al.*[85]	Cobalt-doped titanium dioxide	100 mg of photocatalyst dispersed on a porous quartzose film in the reaction cell, and 3 mL of deionized H_2O and 80 kPa pure CO_2 gas	A 300 W xenon arc lamp with an L-42 glass filter was used as the light source lamp with a cut-off filter (λ > 420 nm)	CH_4 CO H_2 O_2	0.09 μmol g^{-1} h^{-1} 1.94 μmol g^{-1} h^{-1} 0.74 μmol g^{-1} h^{-1} 0.133 μmol g^{-1} h^{-1}	— — — —
33	Yaghoubi *et al.*[86]	Oxygen vacancy and Ti^{3+} originated during synthesis (synthesis form peroxo-titanium complex)	100 mg of photocatalyst + CO_2 bubbled through water, (20 psi pressure), 40 °C	Both solar and visible light 300 W Xe lamp	CH_4 (solar light)	79.5 ppm g^{-1} h^{-1}	0.0289 (250–564 nm)
				Solar light 80 mW cm^{-2}	CO (solar light)	303 ppm g^{-1} h^{-1}	—
				Visible light 408 to 1650 nm	CH_4 (visible light)	60 ppm g^{-1} h^{-1}	—
					CO (visible light)	226 ppm g^{-1} h^{-1}	—
34	Han *et al.*[87]	TiB_2 is used to prepare (self doped) Ti^{+3} in TiO_2	30 mg catalyst was dispersed into 20 mL of *N*,*N*-dimethylformamide and 10 mL ultrapure water	300 W Xe lamp	CO (simulated solar light)	724 μmol g^{-1} h^{-1}	—
					H_2 (simulated solar light)	5.5 μmol g^{-1} h^{-1}	—
					CO (visible light)	58 μmol g^{-1} h^{-1}	—
35	Shi *et al.*[88]	*In situ* pyrolysis of MIL-125-NH_2 (Ti) with melamine	5 mg photocatalyst dispersed in 5 mL of solution of 4 mL of methyl cyanide (MeCN) solvent, 1 mL of (TEOA), bipyridine (bpy) (10 mmol L^{-1}) and 25 μL of 20 mmol L^{-1} $CoCl_2$ purged with CO_2, co-catalyst: $Co(bpy)_3^{2+}$	300 W xenon lamp	CO	388.9 μmol g^{-1} in 5 h	—
				UV cut-off filter (λ > 400 nm)	H_2	75 μmol g^{-1} in 5 h	—
36	Feng *et al.*[89]	During MgO deposition by ALD	10 mg photocatalyst loaded over glass fiber paper, CO_2 passed through water, no co-catalyst	450 W Xe lamp	CO	54 μmol g^{-1} in 4 h	—

which could have resulted in the transfer of an electron from the CB of TiO_2 to the Ni nanocluster and further to the adsorbed CO_2 molecule. The hole remaining on TiO_2 transferred to the water to generate H^+. The enhanced photocatalytic activity and selectivity were attributed to the synergistic effect of Ni nanoclusters and oxygen vacancies on black TiO_2.

To further improve the photocatalytic activity, Fu *et al.*[54] loaded KSCN along with Ni over oxygen vacant TiO_2. The H–Ni–TiO_2 photocatalyst was synthesized by a hydrothermal process, followed by hydrogenation in the presence of pure H_2 gas. At the same time, SCN–H–Ni–TiO_2 was synthesized by modifying H–Ni–TiO_2 with potassium thiocyanate passivation. No structural and morphological changes were observed after modification with KSCN. DRS absorption spectra showed that the absorption in the region of 400–1600 nm decreased after modification with thiocyanate and this could be due to the passivation of surface defects (Fig. 11a). Similar results were observed in the XPS data as no peak corresponding to Ti^{3+} was found after passivation.

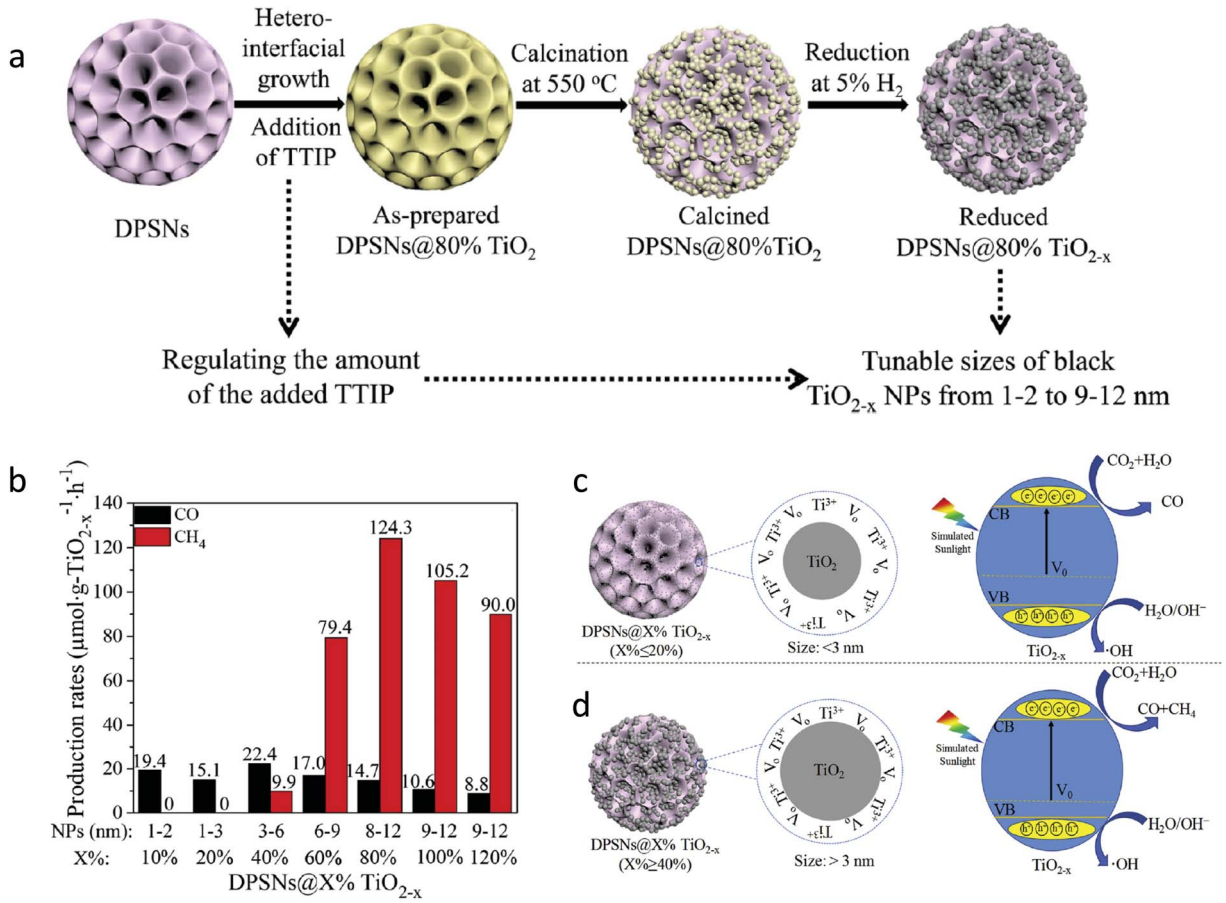

Fig. 9 (a) Synthesis protocol for reduced DPSNs@*X*% TiO_{2-x} NPs, (b) photocatalytic CO_2 conversion using different samples, (c and d) a probable mechanism for the different activity and selectivity of DPSNs@*X*% TiO_{2-x} NPs with the varied particle size of black TiO_{2-x} NPs for CO_2 conversion (reproduced from ref. 52 with permission from Elsevier, copyright 2019).

The SCN–H–Ni–TiO_2 photocatalyst showed the maximum yield of 11.30 and 1.20 μmol g^{-1} in 6 h for acetaldehyde and methanol, respectively (Fig. 11b). Acetaldehyde production was 2.80 times higher than that observed using H–Ni–TiO_2 under solar light illumination. Also, it retained the catalytic activity up to 88% after 40 h of reaction, whereas the H–Ni–TiO_2 sample retained only 40% of the catalytic activity after 10 h of reaction. Thus, modification of KSCN further helped improve the catalytic activity as well as stability. Fig. 11c shows the band alignment derived from UPS and DRS absorption data. The induced interfacial dipole in SCN–H–Ni–TiO_2 shifted the Fermi level as well as the CB and VB edge and also induced an electric field at the interface, which assisted in the separation of charges by driving away hole over the surface. The improvement in activity and stability in the case of SCN–H–Ni–TiO_2 was attributed to the surface passivation and improved charge separation due to the formation of the interfacial dipole.

Similarly, Ye *et al.*[55] synthesized inverse opal (IO) structured three-dimensional nickel loaded black TiO_2 (referred to as IO-B-TiO_2/Ni) from IO-W-TiO_2/NiO *via* the hydrogenation process at 550 °C for 3 h under H_2 atmosphere. The hydrogenation treatment reduced NiO to Ni nanoparticles and Ti^{4+} to Ti^{3+} in TiO_2. EPR and XPS analysis confirmed the presence of Ti^{3+} centres. The IO-B-TiO_2 showed narrow bandgap width and the highest light absorption as compared to P25 because of the slow photon effect of IO structured material and the existence of Ti^{3+} centres (Fig. 12A). They found that the CO production rate of 12.13 μmol g^{-1} h^{-1} using IO-B-TiO_2/Ni under a 300 W Xe lamp was 10.1, 5.1, and 2.0 times higher than that using P25, IO-W-TiO_2 and IO-B-TiO_2, respectively (Fig. 12B). The photocatalyst IO-B-TiO_2/Ni was stable over five cycles. The introduction of Ni and the presence of Ti^{3+} on the outer layer of black TiO_2 both improved the rate of separation of photogenerated e^-–h^+ by trapping of photogenerated electrons *via* a synergistic effect, thus enhancing photocatalytic activity. PL spectra, photocurrent transient response and electrochemical impedance spectroscopy proved that the recombination rate of photogenerated e^-–h^+ was the slowest in the case of IO-B-TiO_2/Ni as compared to P25, IO-W-TiO_2, and IO-B-TiO_2. Under light irradiation, an electron could transfer from the CB of TiO_2 to Ni where adsorbed CO_2 was reduced to CO by accepting photogenerated electrons concentrated on the surface of Ni (Fig. 12C). The improved photocatalytic activity was ascribed to the enhanced light absorption due to the slow photon effect of the IO structure, the formation of a disorder layer and better charge separation efficiency.

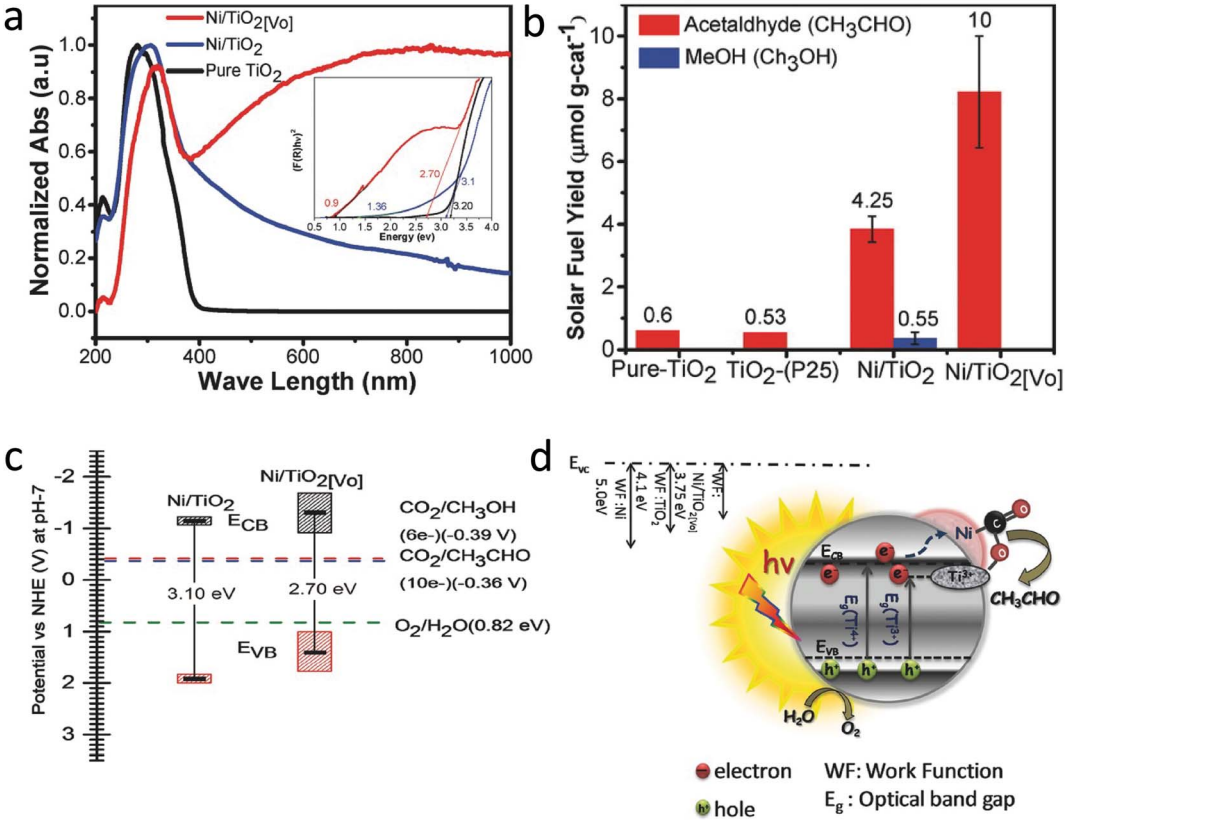

Fig. 10 (a) DRS absorption spectra (inset shows Tauc plots with fitting), (b) the cumulative yield of acetaldehyde for 6 h on pure TiO_2, TiO_2–P25, Ni/TiO_2, and $Ni/TiO_2[V_O]$ using a halogen lamp as a light source, (c) band-edge positions of Ni/TiO_2, and $Ni/TiO_2[V_O]$ estimated using UPS and DRS bandgap and (d) schematic illustration of a mechanism for photocatalytic CO_2 reduction of $Ni/TiO_2[V_O]$. (reproduced from ref. 53 with permission from Wiley, copyright 2018).

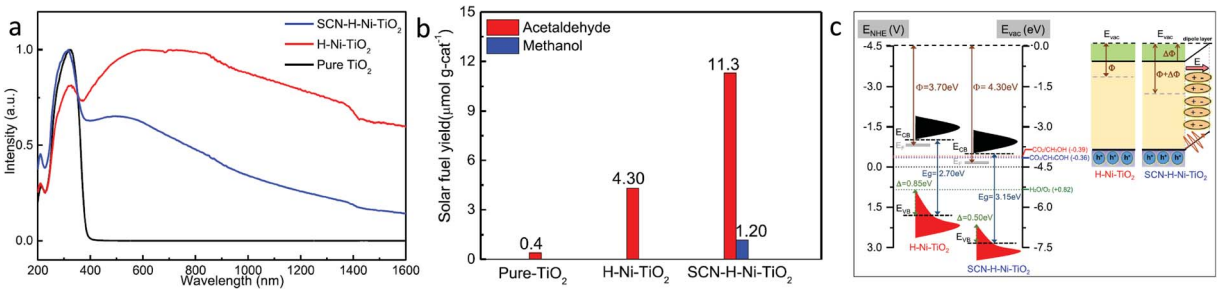

Fig. 11 (a) DRS absorption spectra of the samples, (b) photocatalytic CO_2 conversion yield under light illumination, (c) comparative band diagram and interfacial dipole effect of H–Ni–TiO_2 and SCN–Ni–TiO_2 (reproduced from ref. 54 with permission from the American Chemical Society, copyright 2019 American Chemical Society).

Liu *et al.*[56] compared the photocatalytic properties of the Cu doped TiO_2 sample by calcining it in He and H_2 atmosphere. They synthesized Cu doped TiO_2 by the precipitation method followed by the calcination of the as-synthesized sample in the air at 400 °C. Furthermore, the sample was calcined in He and H_2 atmosphere at 220 °C for 1.5 h. During heat treatment in He and H_2, the formation of defects, namely oxygen vacancies and Ti^{3+}, were found. He and H_2 treated samples formed predominately Cu^{1+} and mixed Cu^{1+}/Cu^0, respectively. The color of the H_2 treated sample was found to be darker and it also showed enhanced absorption in the visible region compared to the He treated sample. This enhancement in the light absorption in the case of the H_2 treated sample was due to the high concentration of oxygen vacancies and the presence of interstitial H. The sample treated in the H_2 atmosphere showed the highest activity for CH_4 and CO generation compared to the He treated samples. The improvement in activity was attributed to the presence of oxygen vacancies and Ti^{3+}, which provided a site for CO_2 adsorption and subsequent transfer of an electron to the adsorbed CO_2. Also, the presence of the Cu^{1+}/Cu^0 redox couple generated by H_2 reduction resulted in higher activity for the trapping of photogenerated electrons and holes than the

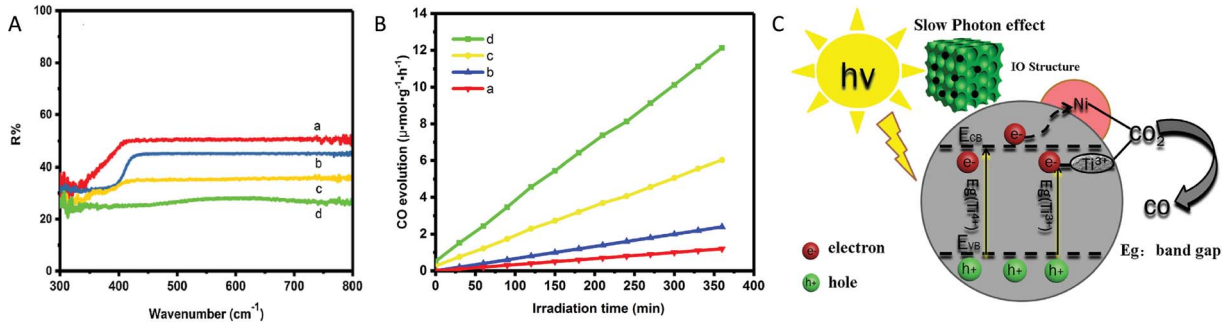

Fig. 12 (A) UV-vis DRS and (B) rate of CO generation during the photocatalytic reduction of CO_2 using (a) P25, (b) IO-W-TiO_2, (c) IO-B-TiO_2 and (d) IO-B-TiO_2/Ni. (C) Schematic representation of the mechanism for photocatalytic CO_2 conversion (reproduced from ref. 55 with permission from Elsevier, copyright 2019).

presence of only Cu^{1+} species induced by He treatment. 1 atom% Cu doped TiO_2 after hydrogen treatment showed the highest activity of 25 and 4.4 μmol g^{-1} in 6.5 h for CO and CH_4 production, respectively.

The impact of hydrogenation before and after metal oxide loading was studied by Li *et al.*[57] They observed that the dispersion of CoO_x over TiO_2 nanotubes varies on changing the sequence of hydrogenation treatment. In this work, nanotubes of TiO_2 with the mixture of anatase and TiO_2(B) phase (referred to as AB) were synthesized. The impregnation method was used to load CoO_x over AB (referred to as (AB-Co)) and then the sample was calcined in the air (referred to as AB-A). The AB-Co sample was calcined in the presence of N_2/H_2 (1 : 9) and referred to as AB-Co-H. In another approach, AB was first calcined in N_2/H_2 and then Co ions were loaded over it by the impregnation method and referred to as AB-H-Co. TEM shows the well-dispersed CoO_x over the TiO_2 nanotubes. It was found that the CoO_x nanoparticles on AB-Co and AB-H-Co were amorphous, while AB-Co-H showed the crystalline CoO nanocrystals. The size of the CoO_x nanoparticles was found to be in the order AB-Co-H > AB-Co > AB-H-Co. The stronger interaction between the oxygen vacancy of TiO_2 and the CoO_x nanoparticles resulted in the high dispersion and smaller size of CoO_x in AB-H-Co as compared to other samples. DRS absorption spectra did not show much change in the absorption edge, indicating the introduction of a smaller number of oxygen defects. d–d transition of Co^{2+} species was observed in the range of 550–670 nm. They compared the CO_2 conversion yield obtained *via* photocatalysis (PT) and photo-thermo-catalysis (PTC). A significant increase in the yield of CO and CH_4 was observed for the reaction carried out photo-thermo-catalytically at 120 °C. The calcined sample of AB-Co showed a lower yield for CH_4. This could be due to the aggregation of the CoO_x after calcination. The highest yield of 16.4 and 10.05 μmol g^{-1} h^{-1} of CO and CH_4 generation was observed in the case of the AB-H-Co sample, respectively. The improved activity was attributed to two factors: the first is the presence of oxygen vacancies, which helped in better charge separation, dispersion of CoO_x and adsorption of CO_2 and the second is the role of CoO_x as the co-catalyst, which acted as a hole trap and enhanced the proton generation form water oxidation.

4.1.2 Using hydrides. The use of hydrides for the generation of defects is an easy and safe method. $NaBH_4$ is used as a source of hydrogen as it has a hydrogen content of 10.66 wt% and decomposes in a single step to give hydrogen.[58] One of the methods to produce defects is heating a mixture of TiO_2 and $NaBH_4$ in an Ar atmosphere. The *in situ* generation of the active hydrogen species creates oxygen vacancies on the surface of TiO_2.

Sorcar *et al.*[59] reported reduced blue titania (referred to as BT) synthesis by mixing P25 TiO_2 with $NaBH_4$ followed by heating at 350 °C for 30 min under an Ar atmosphere. Samples were referred to as BT-*x* where *x* is the amount of $NaBH_4$ in mg used during synthesis for 200 mg of P25 TiO_2. Pt was photo-deposited over the BT-30 sample and the amount of Pt was varied from 0.25–0.5 wt%, and the sample was named *y*-BT-30 where *y* is the amount of Pt. The color of the sample becomes darker, with an increase in $NaBH_4$ content. They found that the treatment of TiO_2 with $NaBH_4$ introduced a shell of a disorder layer over the crystalline core. The enhancement of light absorption in the visible region was attributed to the formation of the disorder surface layer and the existence of Ti^{3+}. The particle size of the Pt was varied from 1.82 nm for 0.25 wt% to 3.5 nm for 0.5 wt%. The highest methane generation at the rate of 80.35 μmol g^{-1} h^{-1} with AQE of 12.4% was observed using 0.35-BT-30 having a Pt content of 0.35 wt% under solar light irradiation with 100% selectivity. The catalytic activity was stable for five cycles. The decrease in activity in the second cycle was due to the saturation of active sites by the adsorption of the intermediate products. Therefore, after the 2nd, 3rd and 4th cycle, the catalyst was subjected to the vacuum treatment to desorb the products from the catalyst surface. The improved yield of 0.35-BT-30 was attributed to the presence of defects, optimum amount and size of Pt nanoparticles, and appropriate band alignment.

To further modify the performance of the catalyst, Sorcar *et al.* decorated the blue titania (referred to as RBT) with graphene.[60] Graphene wrapped RBT samples (G/RBT) were prepared by annealing the graphene oxide-RBT composite (GO/RBT) samples in a vacuum oven at 230 °C for 90 minutes. On this composite, the generation of 77 μmol g^{-1} of ethane (C_2H_6) and 259 μmol g^{-1} of CH_4 in 7 h under solar light illumination

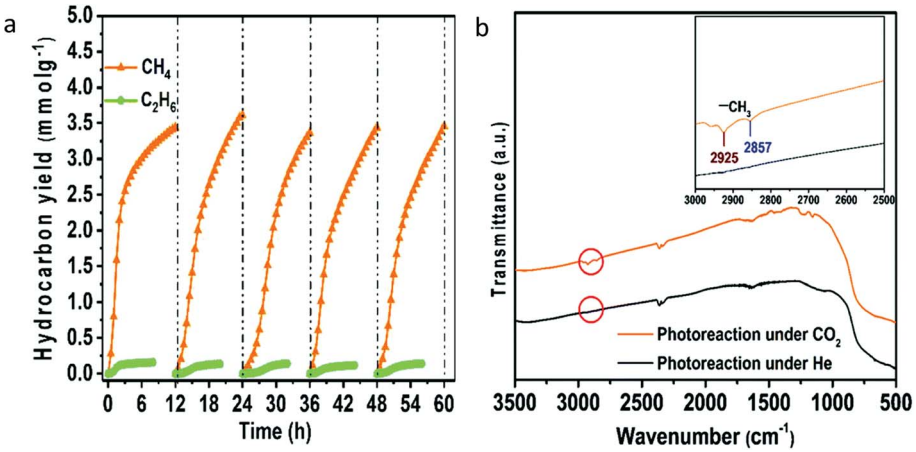

Fig. 13 (a) Stability evaluation of Cu–Pt modified blue titania for photocatalytic CO_2 conversion, (b) FTIR analysis of the sample after photocatalytic reaction carried out in the presence of CO_2 and He gas (reproduced from ref. 61 with permission from the Royal Society of Chemistry, copyright 2019).

with an AQE of 7.9% was observed. The stability of the photocatalyst was evaluated for 42 h. UPS studies revealed the formation of Ti–O–C bonds at the interface, resulting in upward band bending, which was responsible for the hole transfer from RBT to the graphene. The transient absorption spectroscopy studies revealed the accumulation of photogenerated holes and electrons on the graphene and Ti^{3+} sites, respectively. The generation of C1 and C2 products was attributed to the efficient charge separation and accumulation of photogenerated electrons and holes is attributed to the RBT and graphene surface, respectively.

To further improve the performance of blue titania, Sorcar *et al.*[61] deposited Cu and Pt over reduced blue-titania by the photodeposition method to improve the yield of CH_4 and C_2H_6. Photoconversion of CO_2 using 1 wt% of Cu-0.35 wt% of Pt modified blue titania generated CH_4 and C_2H_6 with a rate of 3.0 mmol g^{-1} and 0.15 mmol g^{-1} in 6 h under artificial sunlight illumination with 1% solar to fuel efficiency (SFE) and 86% AQE, respectively. The catalyst was found to be stable for 60 h (Fig. 13a). FTIR spectra of the catalyst recorded after photocatalytic CO_2 conversion showed characteristic signals corresponding to CH_3; this indicated that CH_3 was the intermediate formed during the catalytic reaction (Fig. 13b). They claimed that the Cu nanoparticles provided sites for CO_2 adsorption, while the Pt effectively prevented electron–hole recombination. The improvement of photocatalytic activity was attributed to the synergistic effect between charge separation and transfer from Pt to Cu and the enhanced adsorption of CO_2 by the presence of both oxygen defects and Cu sites.

4.1.3 High energy particle: H_2 plasma treatment. Yan *et al.*[62] synthesized defective TiO_2 by hydrogen plasma treatment at 150 °C using P25 TiO_2. The concentration of defects was varied by varying the plasma treatment time for 30 s, 1 min, 3 min, 5 min, and 20 min and the sample was referred to as H–TiO_2-*x* where *x* is plasma treatment time. It was found that the absorption in the visible region increases with an increase in the time of plasma treatment. This was also evident from the color change of the sample from white to black (Fig. 14a). The increase in disordered layer thickness was observed from 0 to 2 nm while increasing the plasma treatment time from 30 s to 20

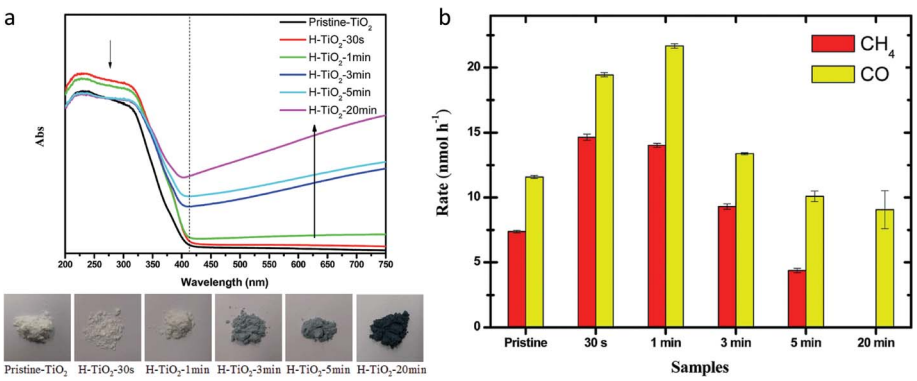

Fig. 14 (a) DRS spectra and the photograph of the samples with increasing plasma treatment time and (b) photocatalytic CO_2 conversion using hydrogenated samples under solar light illumination (reproduced from ref. 62 with permission from the Royal Society of Chemistry, copyright 2014).

min. The 1 min plasma-treated sample showed the highest CH_4 and CO generation at a rate of 14.03 and 21.67 nmol h^{-1} using 90 mg of the catalyst under solar light illumination, respectively (Fig. 14b).

4.2 Defect generation by annealing in an oxygen-deficient atmosphere

4.2.1 Annealing in an inert (Ar, He or N_2) atmosphere. One of the ways to generate the oxygen vacancy in TiO_2 is by thermal treatment in an oxygen-deficient environment such as an He, Ar, or N_2 atmosphere, or vacuum. The generation of oxygen vacancies at a high temperature can be elucidated by the following reversible reaction using standard Kröger–Vink notation:[33]

$$O_O \leftrightarrow V_O + \frac{1}{2}O_2(g) + 2e^- \quad (10)$$

where O_O, V_O, $[V_O]$ and $p(O_2)$ refer to lattice oxygen, oxygen vacancy, concentration of oxygen vacancies and oxygen pressure, respectively.

The equilibrium constant (K) of the above reaction can be given as follows:

$$K = [V_O]n^2p(O_2)^{(1/2)} \quad (11)$$

Rearranging the equation in terms of the concentration of oxygen vacancies can give the following:

$$[V_O] = Kn^{-2}p(O_2)^{-(1/2)} \quad (12)$$

This equation indicates that the concentration of oxygen vacancies will increase with a decrease in oxygen pressure. Thus, thermal treatment in the oxygen-deficient atmosphere facilitates the generation of oxygen vacancies.[33]

Liu *et al.*[63] compared the photocatalytic activity of defective and defect-free anatase, rutile and brookite polymorphs of TiO_2. They introduced defects in the polymorphs by heating them in the flow of He gas for 1.5 h at 220 °C. It was found that heating in the presence of He produces oxygen vacancies and Ti^{3+} ions on the surface of the anatase and brookite form while it is negligible in the case of the rutile phase. *In situ* diffuse reflectance infrared Fourier transform spectroscopy (DRIFTS) studies revealed that the pristine TiO_2 could not activate the CO_2, as no formation of the CO_2^- intermediate occurred over it. Different intermediates were spotted over anatase and brookite forms. The anatase phase formed predominantly CO_2^- as one of the intermediates, whereas brookite showed the formation of both CO_2^- and HCOOH species. It was observed that water adsorption was favored over the brookite surface. Only in the absence of water, characteristics bands of CO_2^- species appeared and the concentration of these species increased with an increase in illumination time, confirming that the CO_2^- species reacted immediately with water to form CO during light irradiation. Also, they found that the brookite phase was more photo-catalytically active as a lower amount of energy was required to produce the oxygen vacancy on its surface as compared to the anatase and rutile phases by using this synthesis protocol. Total production of CO and CH_4 was found to be 18.9 μmol g^{-1} in 6 h under solar light illumination using the defective brookite TiO_2 polymorph in the presence of water vapor. CO was found to be the major product of CO_2 conversion.

Further research was carried out by Xin *et al.*[64] to synthesize the defects over brookite nanosheets of TiO_2, by an oxidation-based hydrothermal method using TiH_2 as a titanium precursor, followed by post-annealing at different temperatures, 300, 500 and 700 °C, in the presence of a N_2 flow. They found that with an increase in calcination temperature, the (concentration of Ti^{3+} decreases) powder becomes brown, black and light grey. The crystallinity of samples also increased with increasing calcination temperature. The fading of color of the sample annealed at 700 °C was attributed to the difficulty in the diffusion of Ti^{3+} with improved crystallinity resulting in a lower concentration of defect centers. The sample annealed at 500 °C with the highest concentration of 0.7×10^{20} spins mol^{-1} of Ti^{3+} showed CH_4 and CO generation at a rate of 11.9 and 23.5 μmol g^{-1} h^{-1} under visible light illumination, respectively. The improvement in the activity was attributed to the Ti^{3+} ion concentration and light absorption properties of the catalyst.

Zhao *et al.*[65] reported the generation of the oxygen vacancy by annealing in a vacuum. To prevent the oxidation of Cu metal, the TiO_2 precursor was coated over Cu metal nanoparticles and annealed in a vacuum (referred as Cu@TiO_2). They observed that the oxygen vacancies were created as a result of annealing

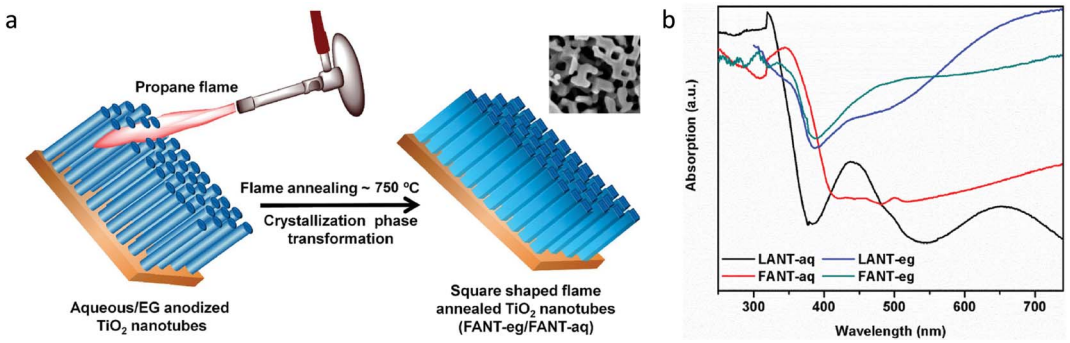

Fig. 15 (a) Synthesis protocol for the generation of oxygen vacancies using propane flame treatment (inset shows TEM image of square-shaped TiO_2 nanotubes after treatment with propane flame) and (b) DRS absorption spectra of LANT-aq, LANT-eg, FANT-aq and FANT-eg samples (reproduced from ref. 66 with permission from Elsevier, copyright 2019).

in a vacuum and their amount increased with an increase in Cu content. The presence of Cu nanoparticles helped form the oxygen vacancies in TiO_2 *via* metal-oxide interactions. This also resulted in improved visible light absorption of Cu@TiO_2. The highest CO and CH_4 production at a rate of 48.5 and 8 μmol g^{-1} in 6 h was observed using Cu@TiO_2 (4 wt% Cu), which was 1.4 times higher than the black TiO_2 under visible light illumination. The improvement in activity was attributed to the enhancement of adsorption of CO_2, light absorption and separation of charge carriers revealed by the transient photocurrent measurements.

4.2.2 Flame reduction method. A flame operates under hydrocarbon-rich and oxygen-deficient conditions, thus providing a reducing atmosphere containing CO and H_2. The annealing of TiO_2 in the reducing atmosphere of a flame generates oxygen vacancies in TiO_2. The flame reduction method offers several advantages, such as high temperature and fast heating rate, allowing the creation of V_O in less than a minute. Kar *et al.*[66] synthesized defective TiO_2 nanotubes by the flame reduction method. In this work, they synthesized defective TiO_2 nanotubes by electrochemical anodization of the Ti electrode in the aqueous and non-aqueous based electrolyte, followed by annealing in the high-temperature flame of a propane torch (750 °C) for 2 min (Fig. 15a). The sample synthesized using the aqueous solution and non-aqueous solution before flame annealing was referred to as LANT-aq and LANT-eg and after flame annealing referred to as FANT-aq and FANT-eg, respectively. They observed that the circular LANT-aq and LANT-eg nanotubes transformed into the square-shaped nanotubes (as shown in Fig. 15a inset) after heating using a propane flame. FANT-aq showed a pure rutile phase while FANT-eg showed a mixture of anatase and rutile phase. The phase transformation, along with thermal stresses during flame annealing at high temperature resulted in the transformation of nanotubes from circular to square-shaped morphology. The square-shaped flame annealed nanotubes showed a higher density of electromagnetic hot spots for visible light and stronger absorption in the UV region than regular nanotubes calcined in the furnace. The presence of Ti^{3+} was confirmed by XPS and EPR studies. Both the flame annealed nanotubes showed the highest light absorption in the visible region due to the generation of localized Ti^{3+} states (Fig. 15b). The FANT-aq and FANT-eg showed methane generation at a rate of 156.5 and 9.5 μmol g^{-1} h^{-1}, respectively. The improvement of activity was attributed to the enhanced light absorption in visible light due to the presence of Ti^{3+}, square morphology, and the presence of both anatase and rutile phases with the (110) plane.

4.3 Using organic reducing agents

Tu *et al.*[67] synthesized the TiO_2/graphene (referred to as G*x*–TiO_2 where $x = 0$, 1, 2, 5 wt% of graphene) hybrid using the simultaneous reduction–hydrolysis method using ethylenediamine and water as a solvent in the hydrothermal treatment. They observed the formation of Ti^{3+} and reduction of graphene from graphene oxide by treatment with ethylenediamine. The light absorption increases with an increase in graphene content, as shown in Fig. 16a. The dispersion of TiO_2 prohibited the restacking of the sheets of the graphene. The nanocomposite with 2 wt% graphene shows the highest rate of 8 and 16.8 μmol g^{-1} h^{-1} of methane and ethane, respectively (Fig. 16b). Initially, the yield of ethane increased with an increase in graphene content. On further increase in graphene content to more than 2 wt%, a decrease in activity was observed which could be attributed to the hindering of light absorption of TiO_2 due to the presence of excess graphene. They attributed the generation of ethane to the synergistic effect between surface Ti^{3+} sites and graphene. Matching energy levels of the d-orbital of TiO_2 and π orbital of graphene and formation of the Ti–O–C bond between graphene and TiO_2 results in d to π orbital overlap; this makes the transfer of the electron from the CB of TiO_2 to graphene possible upon light illumination. This transferred electron could help reduce CO_2 adsorption on the surface. No ethane formation was observed over P25; hence they proposed that electron-rich graphene could stabilize $^{\cdot}CH_3$ radicals and thus help in the formation of methane as well as ethane by coupling of the $^{\cdot}CH_3$ radical.

4.4 Metallothermic reduction

The metallothermic reduction method to generate defects in TiO_2 is easier, safer, and cost-effective as compared to the H_2 reduction method carried out at high pressure and

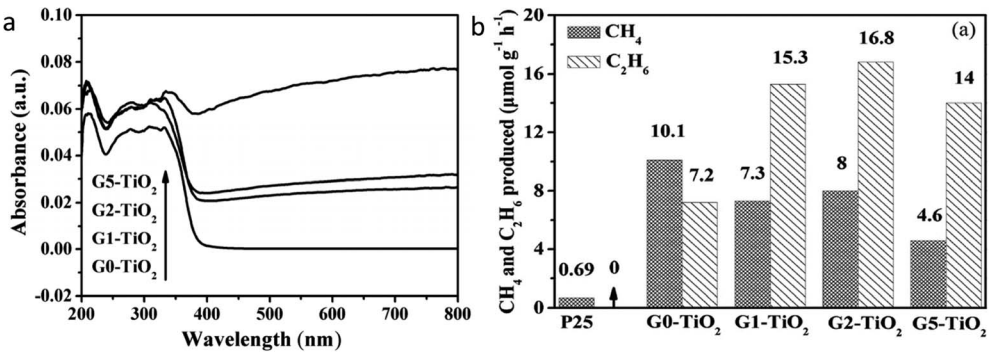

Fig. 16 (a) UV-visible DRS spectrum of G*x*–TiO_2 ($x = 0$, 1, 2 and 5 wt% of graphene) samples and (b) comparison of photocatalytic activity of G*x*–TiO_2 samples in the presence of water vapor (reproduced from ref. 67 with permission from Wiley, copyright 2013).

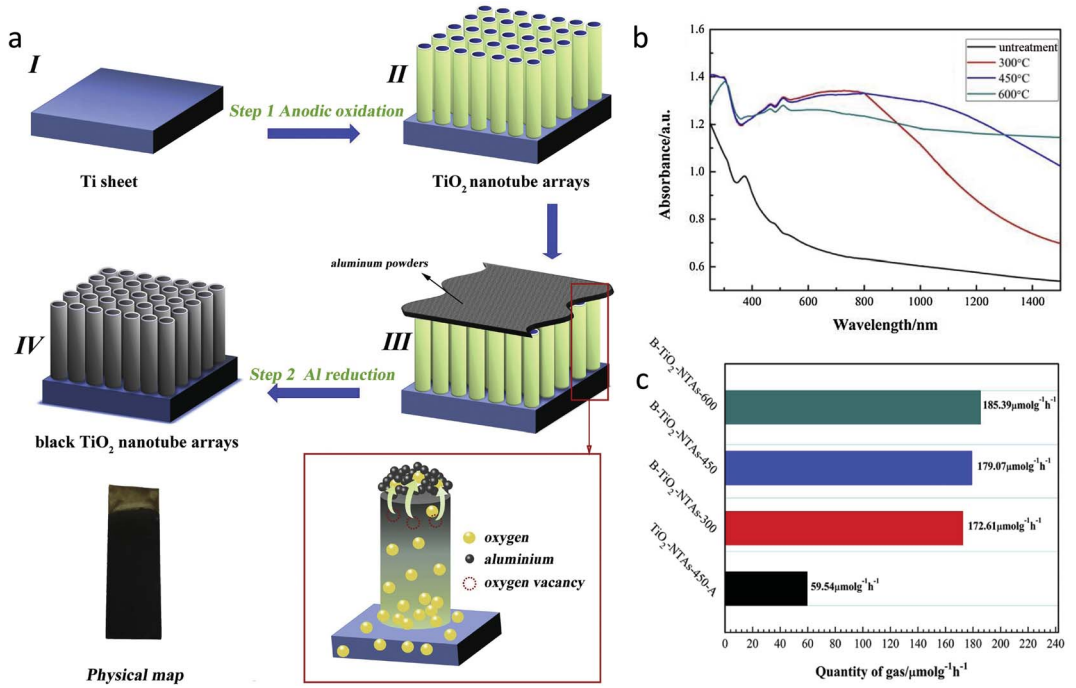

Fig. 17 (a) Schematic of synthesis procedure for the black TiO_2 nanotube array, (b) UV-visible DRS spectra of the sample annealed at different temperatures and (c) photocatalytic CO_2 conversion using different samples under visible light illumination (reproduced from ref. 70 with permission from Elsevier, copyright 2020).

temperature. According to the Ellingham diagram, Al, Mg, and Li possess lower negative potential, and thus can be potential candidates for the reduction of TiO_2.[68] In this method, these metals act as a reducing agent to capture lattice oxygen effectively.

4.4.1 Aluminothermic reduction. Yin *et al.*[69] used Al metal for the generation of defects along with a defective core–shell structure with a crystalline core surrounded by an amorphous layer. They synthesized TiO_2@TiO_{2-x} using a two-zone furnace in which Al and TiO_2 were placed in a different zone and evacuated to a pressure <0.5 Pa. Al was heated at 800 °C, whereas the temperature of TiO_2 was varied from the 300–500 °C to study the impact of the oxygen defect (V_O) and disordered shell on the photocatalytic activity of TiO_{2-x}. It was observed that with an increase in temperature from 400 (referred to as 400-TiO_{2-x}) to 500 °C (referred to as 500-TiO_{2-x}), the amorphous layer thickness increased from 1–2 to 2–3 nm. Also, the oxygen defects and Ti^{3+} increased with an increase in heating temperature, as confirmed by EPR. With an increase in defects, the absorption in the visible region enhanced with a marked change in color of the sample from blue to black. The CO_2 temperature-programmed reduction profile showed that the amount of CO_2 adsorbed over 500-TiO_{2-x} was more than that of pristine TiO_2. The photocatalytic CO_2 conversion was evaluated at 2 bar CO_2 pressure under different sources of light. The highest CH_4 generation at a rate of 14.3 μmol g^{-1} h^{-1} with 74% selectivity was found using 500-TiO_{2-x} under simulated solar light. The 500-TiO_{2-x} catalyst showed considerable methane yield under visible and IR light illumination, whereas pristine TiO_2 did not show any activity under similar photocatalytic conditions. They found that the photothermal effect was not very pronounced as the photocatalytic activity at 50 °C was lower than the activity evaluated at room temperature. Increased oxygen defects and Ti^{3+}, narrowed bandgap, and pronounced surface electronic modification contributed positively to the enhancement of photocatalytic activity.

Also, the oxygen vacancies in TiO_2 were induced by thermal treatment of a mixture of aluminum powder and TiO_2. Gao *et al.*[70] synthesized black TiO_2 nanotube arrays (B–TiO_2 NTAs) by annealing TiO_2-NTAs wrapped with Al powder in an argon atmosphere at temperatures of 250, 300, 450, and 600 °C (Fig. 17a). The obtained samples were named B–TiO_2 NTAs-*x*, where *x* is the temperature. No doping of Al in TiO_2 was observed. The presence of a high concentration of oxygen vacancies introduced by the aluminothermic reduction process and the resultant Ti^{3+} centres creates a defect energy level below the CB of TiO_2; thus, B–TiO_2 NTAs exhibited strong visible light absorption as compared to TiO_2 NTAs (Fig. 17b). The concentration of oxygen vacancy defects was increased with an increase in temperature. The formed oxygen vacancies could act as electron traps; hence B–TiO_2 NTAs showed a lower charge recombination rate than TiO_2 NTAs. To know the effect of oxygen vacancies on CO_2 conversion, they also synthesized NTAs-450-A by annealing TiO_2 NTAs at 450 °C in the air. It was observed that B–TiO_2 NTA samples exhibited better performance in photocatalytic reduction of CO_2 than TiO_2 NTAs-450-A. Among the synthesized photocatalysts, B–TiO_2 NTAs-600 demonstrated the

best performance under visible light irradiation with a CO yield of 185.39 μmol g^{-1} h^{-1}, which could be due to the presence of a large amount of oxygen vacancies in TiO_2 NTAs, lower charge carrier recombination, and abundant sites for the photocatalytic CO_2 reduction (Fig. 17c). The catalyst was 95% active for CO_2 reduction even after five cycles of testing.

4.4.2 Lithiothermic reduction. In this method, defects can be generated at a relatively lower temperature as compared to that required using Al or Mg metal. Li metal is very reactive because of its lower negative potential.[71] Recently, Wang *et al.*[72] generated oxygen defects in anatase TiO_2 nanoparticles using a lithiothermic reduction approach (Fig. 18a), where they used molten Li (at 200 °C) to create defects. They performed the reduction of the anatase phase of TiO_2, by varying the ratio of Li/TiO_2 from 0–20 wt% to synthesize oxygen-deficient R–TiO_2 nanoparticles. The color of the sample changed from white to gray to black with an increase in Li/TiO_2 ratio. They observed that in the lithiothermic reduction method, along with the introduction of oxygen defects, lithium ions also get incorporated into the lattice of TiO_2. At a higher ratio of Li/TiO_2, a cubic phase of $LiTiO_2$ was observed (Fig. 18b). The bandgap varied from 3.3 to 2.4 eV for the different oxygen-deficient R–TiO_2 nanoparticles. The presence of oxygen deficiency and Ti^{3+} species was confirmed from EPR spectra of the R–TiO_2 samples. Electron energy loss spectroscopy (EELS) spectra recorded at the edges and center showed that edges were deficient of Li whereas the presence of Li was observed at the center of the nanoparticle (Fig. 18c and d). 1 wt% Pt decorated R–TiO_2 obtained using 5 wt% Li/TiO_2 ratio showed CH_4 and CO at a rate of 8.85 and 3.49 μmol g^{-1} in 8 h under UV-visible light illumination, respectively. Charge difference distribution over the (101) plane of anatase phase of TiO_2 showed that the oxygen defects act as a center for the CO_2 adsorption and activation. The CO_2 adsorption

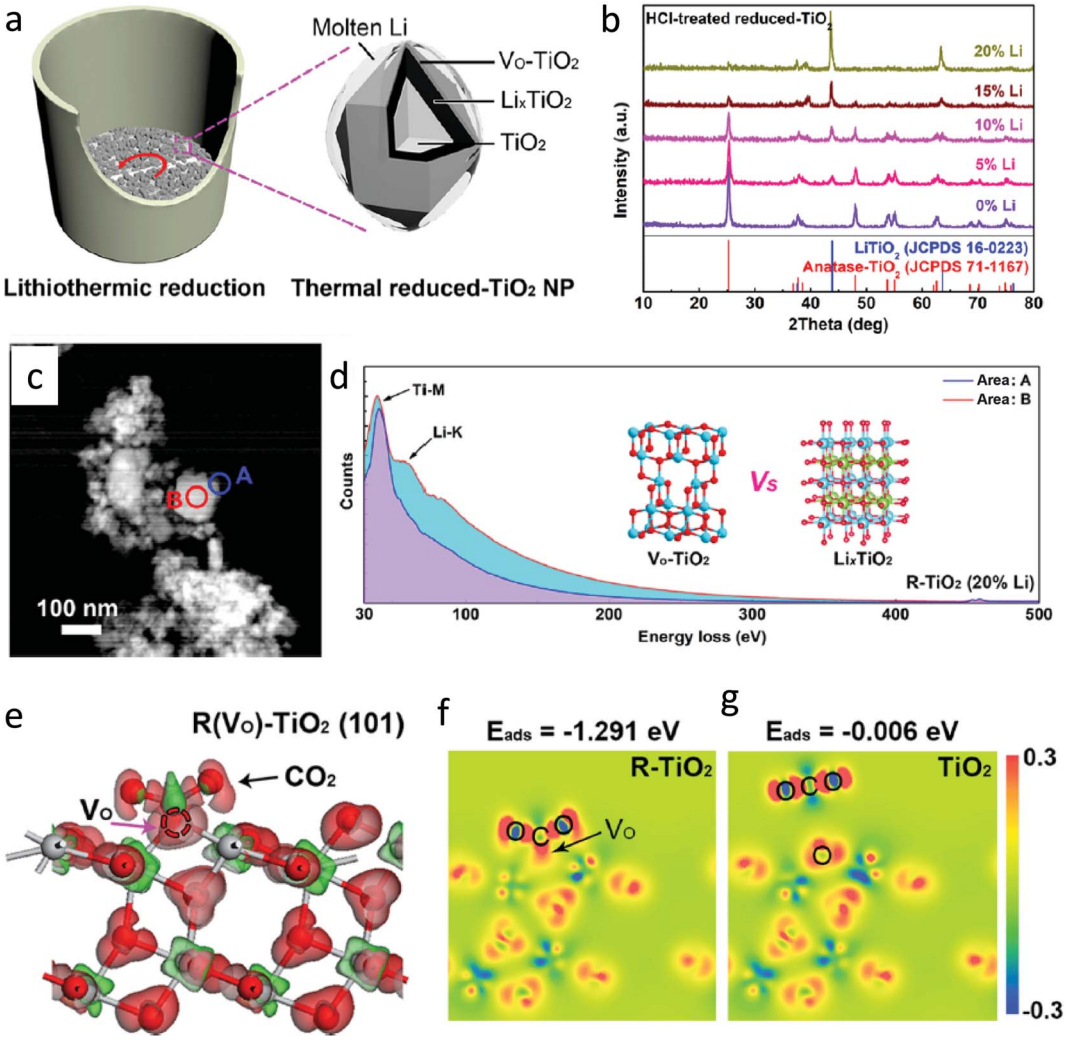

Fig. 18 (a) Synthesis of defective TiO_2 by lithiothermic reduction, (b) XRD spectra of samples synthesized by varying the amount of Li, (c) HAADF-TEM image of R–TiO_2 (20% Li), (d) EELs spectra recorded at the edge position A and center position B; inset shows the atomic structure of oxygen-deficient TiO_2 and cubic Li_xTiO_2, (e) charge difference of the CO_2 molecule adsorbed on the surface of the (101) plane for anatase phase of R–TiO_2 (gray: Ti atom, red: O atom), and (f and g) differential charge density after CO_2 adsorption (reproduced from ref. 72 with permission from the American Chemical Society, copyright 2020).

energy was found to be −1.291 eV over defect sites of R–TiO_2 lower than on the bare TiO_2 (−0.006 eV) (Fig. 18e–g). This further confirmed the role of defects in CO_2 activation and conversion.

5. Defect generation by morphology and facet engineering

Facet engineering is one of the aspects adopted to improve charge separation and thus enhanced photocatalytic CO_2 conversion. The particular facet of the crystal possesses unique electronic properties due to the specific atomic arrangement and coordination, which may affect the adsorption of the reactant, stabilization of intermediates and desorption of the product. TiO_2 with different facets has been reported to carry out different oxidation and reduction reactions on different facets. Generally, the hydrothermal method is adapted to synthesize faceted TiO_2 along with the introduction of Ti^{3+} vacancies or oxygen defects.

It was observed that not only the presence of defects but also the particular morphology assists in improving the yield of photocatalytic CO_2 conversion. Sasan *et al.*[73] reported self-doped rutile TiO_2 (Ti^{3+}–TiO_2) with facets synthesized using the hydrothermal method in the presence of HCl. Fig. 19a shows the SEM images of the Ti^{3+}–TiO_2 sample. Ti^{3+} concentration in self-doped TiO_2 was reported to be ≈4.5 μmol g^{-1}. They claimed the formation of Ti^{3+} in bulk as the XPS did not show any peak corresponding to Ti^{3+}, whereas EPR showed the presence of Ti^{3+} (Fig. 19b). To improve the activity of self-doped TiO_2, Pd and Cu were photodeposited (referred to as Cu^I/Pd/Ti^{3+}–TiO_2) and evaluated for its potential for CH_4 generation from CO_2 and water in the presence of visible light. Fig. 19c shows the TEM image of Cu^I/Pd/Ti^{3+}–TiO_2, which showed the presence of the co-catalyst on the {110} facets. This confirmed that the photogenerated electrons accumulated preferentially at the {110} facets than the {111} facets. The generation of ∼1 μmol g^{-1} h^{-1} CH_4 was observed under visible light illumination (Fig. 19d). To evaluate the impact of the shape and morphology, self-doped TiO_2 was synthesized by the combustion method. CH_4 productivity of Ti^{3+}–TiO_2 synthesized by the hydrothermal method was 2.5 times more than that of the sample synthesized by the combustion method and improvement in activity assigned to the structural features like morphology and facets. The electrons and holes were trapped at different facets such as {111} and {110} of the rutile TiO_2 phase, respectively, thus resulting in improved separation of charge carriers and photocatalytic activity.

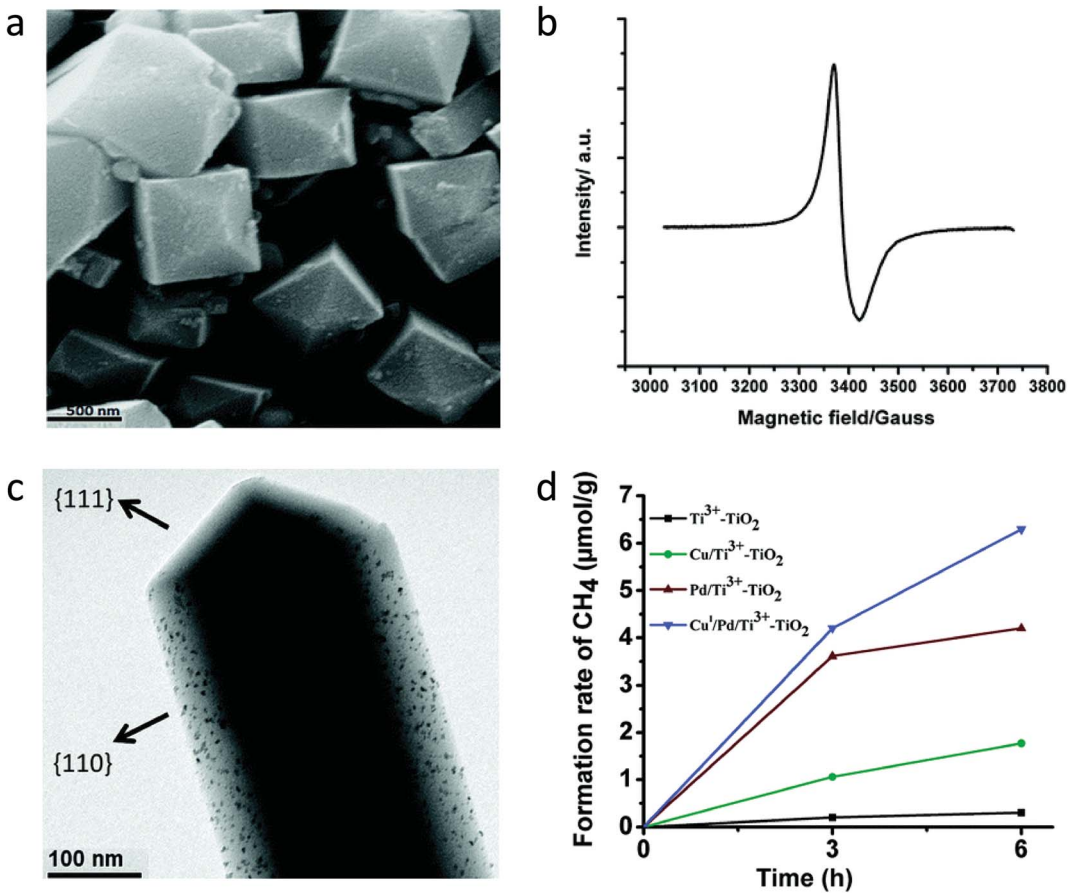

Fig. 19 (a) SEM image of the Ti^{3+}–TiO_2 sample and (b) EPR spectra of the Ti^{3+}–TiO_2 sample recorded at 100 K, (c) TEM images of the Cu^I/Pd/Ti^{3+}–TiO_2 sample, and (d) comparison of photocatalytic CO_2 conversion using different samples (reproduced from ref. 73 with permission from the Royal Society of Chemistry, copyright 2015).

It was observed that the sample synthesized by hydrothermal treatment using HF showed the incorporation of fluoride ions into the lattice of TiO_2 because of its smaller size. The presence of this fluoride ion induces the disordered layer, which further assists in preventing the Ti^{3+} oxidation in the air.[74] Fang *et al.*[74] synthesized deep blue colored reduced TiO_{2-x} *via* a one-step hydrothermal process using HCl and the Ti(III)Cl_3 precursor. During synthesis, a small amount of HF was also added, which resulted in the introduction of a disordered layer, increase in the content of the anatase phase of TiO_2 and structural morphology with the {101} and {001} facets. The samples were referred to as TiO_{2-x} followed by the amount of HF added. The presence of fluoride ions was verified by XPS and HRTEM-EDS. EDS elemental mapping further confirmed that fluoride ions were homogeneously dispersed in the catalyst. Because of the size and charge of fluoride ions, the transformation of the anatase to the rutile phase gets prohibited. The light absorption in the visible region increased with an increase in fluorination and showed the highest absorption for TiO_{2-x}-0.5 (Fig. 20a). This light absorption could be due to the presence of Ti^{3+} and oxygen vacancies. The presence of Ti^{3+} ions was also confirmed by the EPR spectra and showed the presence of 24.6×10^{19} spins per g in TiO_{2-x}-0.50, which was nearly 14 000-fold more as compared to the pristine TiO_2 (Fig. 20b and c). Fig. 20d and e show the HR-TEM image of the TiO_{2-x}-0.5 sample and shows the presence of the {101} and {001} facets.

The presence of the disordered layer of 1–2 nm on the surface of TiO_{2-x} induced by the fluoride atoms prevents the oxidation of Ti^{3+} ions. The presence of facets promotes the separation of electrons and holes as they prefer to accumulate at the {101} and {001} facets, respectively. Photocatalytic CO_2 conversion carried out in the absence of the cocatalyst and under simulated solar light illumination generated CH_4 and CO. The selectivity for CH_4 evolution increased from 51.7% to 83.4% after fluorination (Fig. 20f). The improved photocatalytic performance was attributed to the enhanced solar light absorption by the presence of the Ti^{3+} ion, improved activation of CO_2 by the induced oxygen vacancies and the slow recombination rate because of migration of photogenerated charges on different facets.

Similarly, Liu *et al.*[75] synthesized TiO_2 with co-exposed facets of {001} and {101} by the hydrothermal method using titanium isopropoxide and a small amount of HF. Defects were created by heating a TiO_2 and $NaBH_4$ mixture at 300 °C. The highest yield for CO generation obtained was 54.5 μmol g^{-1} in 5 h under UV-visible light with an AQE of 0.31%. The improved activity is attributed to the electron transfer between the {001} and {101} planes and enhanced light absorption due to the formation of the Ti^{3+} states within a bandgap of TiO_2. *In situ* DRIFTS studies confirmed that the presence of Ti^{3+} along with co-exposed facets of {001}–{101} helped in the activation and conversion of CO_2.

Similarly, Liu *et al.*[76] synthesized ultrathin nanosheets with a thickness of ~0.8 nm (approximately two atomic layers thick) of TiO_2 with abundant facets by the hydrothermal method using ethylene glycol. EPR and XPS studies indicated that the concentration of Ti^{3+} increased after irradiation with UV-visible light. Pt deposited ultrathin TiO_2 exhibited excellent photocatalytic activity for the conversion of CO_2 into CH_4 and CO with a yield of 66.4 and 54.2 μmol g^{-1} h^{-1}, respectively. The improved photocatalytic activity was attributed to the increased surface area and defect sites, which assisted in the charge transfer to well-dispersed Pt nanoparticles and reduced the

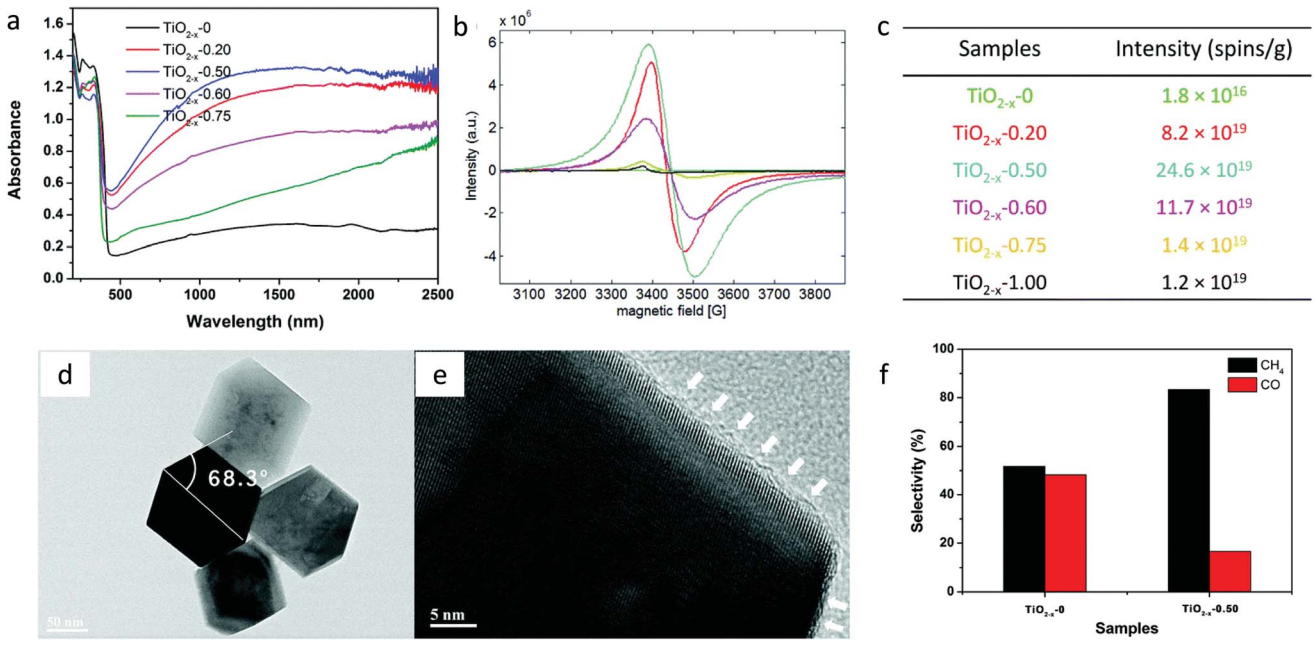

Fig. 20 (a) DRS absorption spectra, (b) EPR spectra and (c) the spin intensity of reduced TiO_2 samples, (d) HRTEM image of TiO_{2-x}-0.50, (e) disordered layers on the surface of TiO_{2-x} marked with white color arrows and (f) selectivity for CH_4 and CO generation using TiO_{2-x}-0 and TiO_{2-x}-0.50 in the absence of the cocatalyst and under simulated solar light (reproduced from ref. 74 with permission from the Royal Society of Chemistry, copyright 2017).

recombination of charge carriers, and the synergy between metal and support helped in the adsorption of CO_2.

It is difficult to generate a defective layer over the particular facets of the photocatalyst by the methods discussed above and, hence, to study its impact on photocatalytic CO_2 conversion. Recently, Shi *et al.*[77] adopted a mild reducing condition to study the role of the formation of the defective layer, particularly on the {001} facets of TiO_2 nanocrystals. The synthesis was carried out in a two-step reduction process *viz.*, the first involves the solvothermal method using TiO_2, $NaBH_4$ and glycol and the second step involves calcination under Ar flow at 400 °C. Fig. 21a–c shows HRTEM images of the TiO_2 homojunction formed after reduction treatment, showing a truncated octahedral bipyramid consisting of the {101} facets on the side and the {001} facets on top and bottom. HRTEM images indicated that the defective layer forms only on the {001} facets and not on the {101} facets. They observed the formation of a heterojunction between the defective layer, interface layer and the crystalline core. HAADF images showed a disordered layer on the {001} facets (Fig. 21d and e). The EELS spectra were recorded at different depths to know the distribution of Ti^{3+} and Ti^{4+} species on the {001} facets (Fig. 21f). Until the depth of 2 nm, the characteristic signals of Ti^{3+} appeared, confirming its presence in the defective layer. In between 2 and 3 nm, the presence of both Ti^{3+} and Ti^{4+} appears, confirming their co-occurrence in the interface layer. After 3 nm depth, the existence of Ti^{4+} in the crystalline layer was observed. EELS spectra confirmed the presence of Ti^{3+} in the defective and interface layer of thickness nearly 2 and 1 nm, respectively. *In situ* DRIFTS study performed in the dark and in thepresence of CO_2 saturated with water vapor further confirmed that CO_2 was activated by forming $CO_2^{\bullet-}$ species on the surface, which was easy to reduce further. Methane was produced at a rate of 2.49 μmol g^{-1} h^{-1} with 100% selectivity under UV light (λ = 365 nm), in the absence of a cocatalyst. The catalyst was found to be stable even after 60 h of a run. The holes are supposed to accumulate on the {001} surface, but they observed that due to the formation of the electron-rich defective layer, the reduction of CO_2 has occurred over the {001} facets and oxidation over the {101} facets.

Similarly, Qingli *et al.*[78] synthesized a porous black TiO_2 film by hydrothermally treating a Ti plate in H_2O_2 solution. The oxygen-deficient nature of the black TiO_2 film was confirmed by the EDX. They monitored photocatalytic CO_2 conversion using simulated sunlight in the presence of moist CO_2 with the production of CO and CH_4 at a rate of 115 and 12 μmol g^{-1} h^{-1} respectively.

An attempt was also made to further enhance the light absorption by using the light trapping property of the hollow microstructure synthesized by the hydrothermal method. Liu *et al.*[79] synthesized the porous fluorinated TiO_2 hollow microstructure (referred to as THMs) with exposed {001} facets and induced defects by hydrothermal treatment using $Ti(SO_4)_2$ and NH_4F. Au was photodeposited on THMs by varying its amount from 0, 0.5, 1, 2 and 4 wt% and referred to as Au_x/THMs where x is the weight ratio of Au to Ti. They found that photodeposition of Au on the THMs increases both the oxygen vacancy and Ti^{3+},

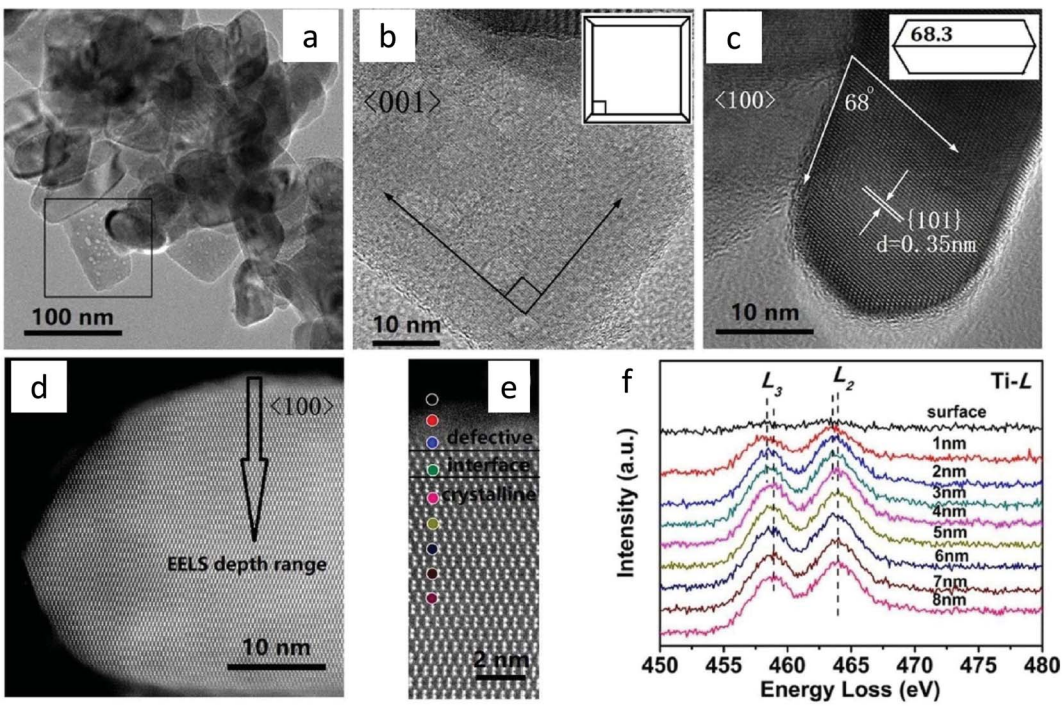

Fig. 21 (a) TEM image of the TiO_2-homojunction, HRTEM image recorded from (b) <001> orientation, inset shows the model of truncated octahedral bipyramid projected along <001> direction, and (c) <100> orientation inset shows the model of truncated octahedral bipyramid projected along <100> direction, (d) HAADF-STEM image recorded from <100> orientation, (e) position for signal collection for EELS spectra, (f) Ti-L spectra recorded at the different positions marked with colored dots in (e) (reproduced from ref. 77 with permission from Wiley, copyright 2019).

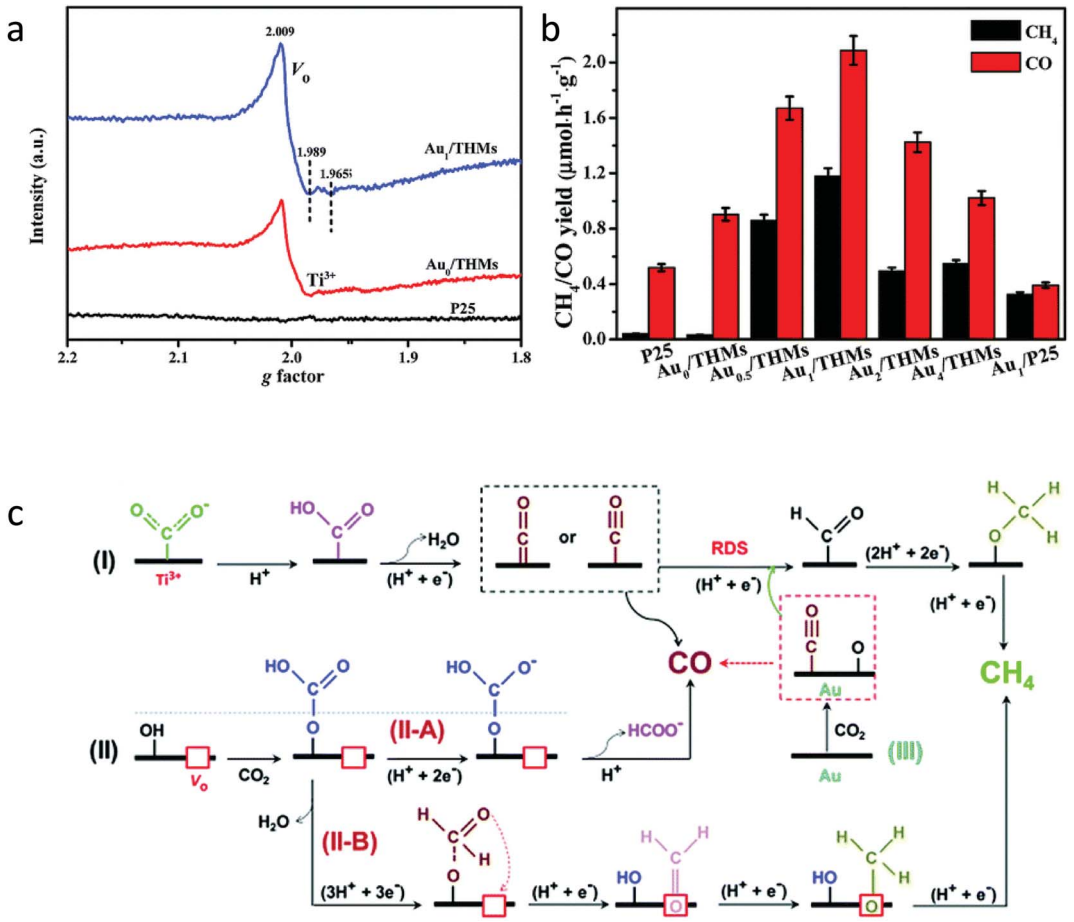

Fig. 22 (a) EPR spectra of P25, Au_0/THMs, and Au_1/THMs, (b) photocatalytic CO_2 conversion over different samples under full-spectrum light illumination and (c) probable mechanism pathway for CO_2 to CH_4 conversion (reproduced from ref. 79 with permission from the Royal Society of Chemistry, copyright 2018).

which further helps adsorb and activate the CO_2 molecule (Fig. 22a). The formation of Ti–F species, surface Ti^{3+} and oxygen vacancies helps in trapping the surface photogenerated charge carriers, thus reducing surface recombination. The improved light absorption was attributed to the light trapping effect of the hollow sphere and surface plasmon resonance (SPR) effect of the Au nanoparticles. The photocatalytic activity for CO_2 conversion enhanced due to improved charge separation as a result of the Schottky junction between Au and TiO_2 and the {001}/{101} facet junction and increased CO_2 adsorption due to the strong affinity of Au nanoparticles to CO_2 as well as the presence of surface Ti^{3+} and V_O sites. Methane formation was favored over the Au_1/THMs due to the strong affinity of CO to Au, which restricted its escape from the surface and helped to further hydrogenate the surface-bound CO to form methane. The maximum yield for CH_4 and CO was 1.19 and 2.10 μmol g^{-1} h^{-1} under UV-visible light irradiation, respectively, using Au_1/THMs (Fig. 22b). *In situ* DRIFTS studies performed using Au_1/THMs revealed that even in the absence of light, species like monodentate and bidentate carbonate, bicarbonate, carboxylate (CO_2^-), and carbon monoxide were formed. CO_2^- species were formed as a result of the presence of oxygen defects and Ti^{3+} sites. Under LED light illumination, the species like bicarbonate, CO_2^- and CO depleted and new species like formate, formaldehyde, dioxymethylene and methoxy groups appeared and became stronger with time. They proposed the possible pathways to generate CO and CH_4 (Fig. 22c): (i) a surface Ti^{3+} (or oxygen vacancy (V_O))-bound CO_2^- activated reaction pathway, (ii) a surface hydroxyl (OH)-bound HCO_3^- derived reaction pathway and (iii) Au-bound CO initiated hydrogenation to produce CH_4.

Another approach was adapted by Yin *et al.*[80] for the synthesis of hydrogenated blue H–TiO_{2-x} by a facile low-temperature solvothermal method using Li-dissolved ethanediamine. During the solvothermal reaction, the generated Li species and [H] atom after mixing of Li metal and ethanediamine were capable of reducing TiO_2 by introducing surface defects and intercalated H. The sample was referred to as H–TiO_{2-x}-*y* where *y* represents the amount of Li in mg. It was observed that the thickness of the disordered layer increases with an increase in the Li content, *i.e.* it changed from 2–3 nm for H–TiO_{2-x}-200 to 4–6 nm for H–TiO_{2-x}-300 (Fig. 23A). ^{1}H NMR spectra of the samples showed the presence of protons in a different environment. It was observed that during the solvothermal process, more H atoms were incorporated at the bridging sites in the amorphous layer (Fig. 23B). The kinetic

isotope effect studies indicated that the breaking of the C–O bond of CO_2 was the rate-determining step in photocatalytic CO_2 conversion rather than the O–H bond of H_2O. Fig. 23C shows the *in situ* DRIFTS performed in the dark as well as under light illumination to study the reaction intermediates. The amount of the different carbonate species increases with an increase in illumination time over the surface of H–TiO_{2-x}. The *in situ* DRIFTS measurements confirmed the formation of the intermediate of CO_2^- which indicated that CO_2 gets adsorbed and activated on the surface of defective H–TiO_{2-x}. CO_2 conversion into methane at a rate of 16.2 and 2.7 μmol h^{-1} g^{-1} with a selectivity of 75 and 77% were observed using H–TiO_{2-x}-200 under solar light and visible light illumination (400–780 nm), respectively. It was found that the increase of thickness of the disorder layer to 4–6 nm in H–TiO_{2-x}-300 was not favorable for the transport of photo-generated charge carriers, which resulted in low photocatalytic activity.

6. Defect generation during synthesis, doping and composite formation

The formation of defect during the synthesis of the catalyst and its application for the CO_2 conversion is discussed in this

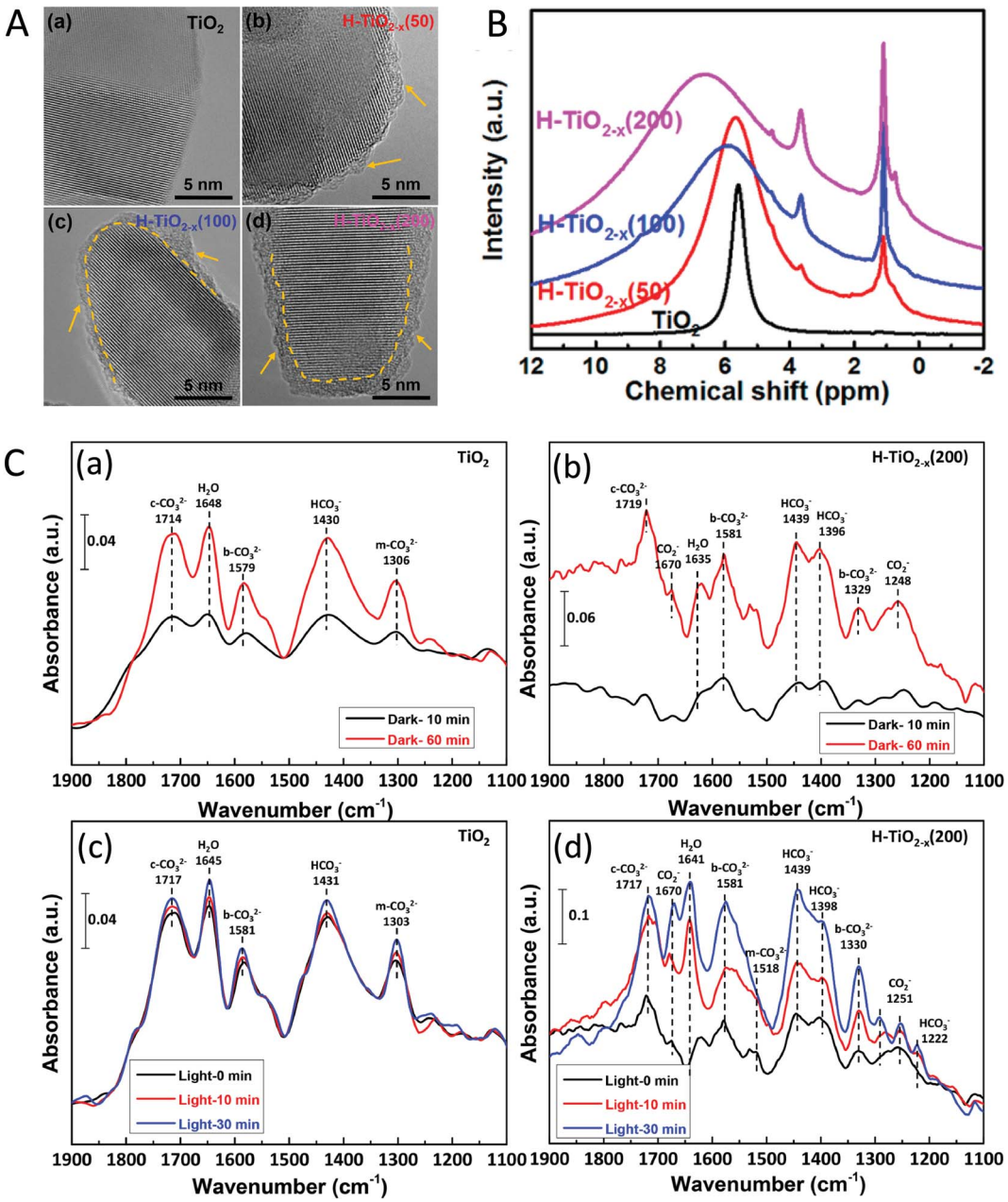

Fig. 23 (A) HRTEM images of the TiO_{2-x} with different amounts of Li, (B) ^{1}H NMR spectra of the defective blue H–TiO_{2-x} samples, (C) *in situ* DRIFTS spectra monitored in the dark for (a) TiO_2 and (b) H–TiO_{2-x}-200 and after shining light for (c) TiO_2 and (d) H–TiO_{2-x}-200 (reproduced from ref. 80 with permission from the American Chemical Society, copyright 2018).

section. The defects were also found to generate during the photodeposition process. Zhu *et al.*[81] studied the impact of defects generated during photodeposition of Cu_2O. They synthesized the nanosheets of TiO_2 with facets of {001} by the hydrothermal method and Cu_2O was deposited over it by the photodeposition method (referred to as Cu–TiO_2-*x*, where *x* is the wt% of Cu species). During *in situ* photodeposition, along with Cu deposition, oxygen vacancies were also generated on the surface of TiO_2 nanosheets. The EPR spectra revealed that the intensity of V_O after deposition of Cu_2O increased, whereas the intensity of Ti^{3+} decreased significantly (Fig. 24A). The decrease in Ti^{3+} signal indicated that the Cu^{2+} adhered to the Ti^{3+} sites where it was reduced to Cu^{1+} by accepting an electron from Ti^{3+}. Fig. 24A(b) indicated that after the introduction of CO_2, the oxygen defects decreased, whereas the Ti^{3+} remains the same. This further confirmed that the V_O acts as CO_2 adsorption centers and the formation of $CO_2^{\bullet-}$ sites on the surface of the Cu–TiO_2-1. The presence of Cu_2O increases the alkalinity and forms oxygen defects (V_O), thus leading to improvement of adsorption of CO_2 over Cu–TiO_2-1 as compared to pristine TiO_2 (Fig. 24B).

In situ FTIR spectra recorded under light illumination showed that the intensity of the $CO_2^{\bullet-}$ species increases with an increase in light illumination (Fig. 24C). The decrease in the water absorption band indicated its consumption during the reaction. Methane yield was found to be dependent on the concentration of Cu_2O. The highest methane yield of 8.68 μmol g^{-1} h^{-1} was observed with 100% selectivity using 1 wt% of Cu(I) species under simulated solar light illumination and in the presence of CO_2 and H_2O vapor (Fig. 24D). On further increase in the Cu_2O amount, active species decreased due to its aggregation. Surface V_O and Cu^{1+} act as active centers for the conversion of CO_2 into methane. The enhancement of photocatalytic activity was attributed to high CO_2 adsorption capacity, high electron mobility, and high concentration of V_O. Based on the experimental results, they proposed a plausible mechanism for methane production, as shown in Fig. 24E. $CO_2^{\bullet-}$ was formed by accepting the electron from V_O site. The photogenerated electron in the presence of atomic hydrogen was used for the reduction of $CO_2^{\bullet-}$ species to give methane over the Cu^{1+} sites of Cu–TiO_2-*x*.

Lan *et al.*[82] reported the defects induced during the loading of Cu. They synthesized a series of ultrafine highly crystalline metallic Cu nanoparticles deposited TiO_2 *via* a solvothermal method using alcohol (referred to as Cu/TiO_2). The defects induced by the introduction of Cu during the synthesis decreased the bandgap of Cu/TiO_2 (Fig. 25a). They found that CO was the only product formed during photocatalytic CO_2 reduction using Cu/TiO_2. The 0.5 wt% Cu/TiO_2 catalyst produced 32.5 μmol g^{-1} h^{-1} of CO, which was 5.2 times higher as compared to pure TiO_2 under irradiation of UV-visible light (Fig. 25b). The high activity and selectivity could be attributed to the oxygen vacancies in Cu/TiO_2 catalysts. Importantly, the Cu/TiO_2 catalyst stopped producing hydrogen after 2 h of light irradiation, whereas CO yield increased continuously with irradiation time. DFT calculation showed that the adsorption energy of CO on the Cu surface was much higher than that of H_2 (Fig. 25c). Hence, with increasing reaction time, the accumulated CO species occupied the Cu surface and prevented the access of H ions to the Cu surface, resulting in the suppression

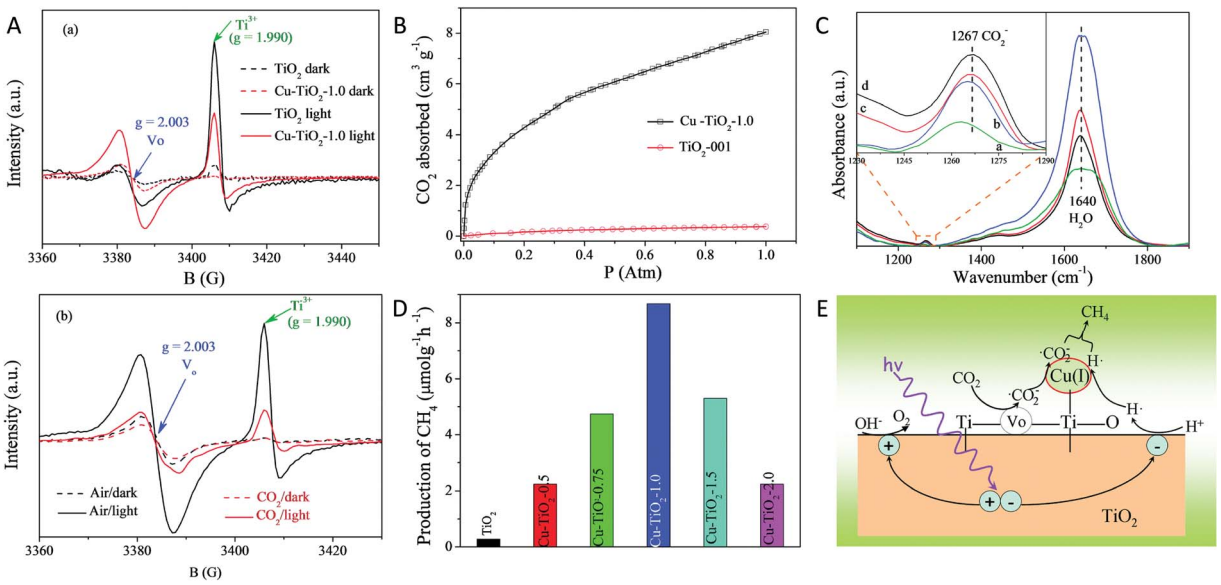

Fig. 24 (A) (a) EPR spectra of TiO_2 and Cu–TiO_2-1.0 samples recorded under vacuum at 77 K in the dark and after solar light illumination, (b) EPR spectra of the Cu–TiO_2-1.0 catalyst in the presence of air and CO_2, (B) CO_2 adsorption isotherm of TiO_2 and Cu–TiO_2-1.0 samples, (C) *in situ* FTIR spectra recorded in the presence of CO_2 and H_2O, (a) raw Cu–TiO_2-1 sample (b) after 30 min in the dark, (c) after 30 min of light illumination and (d) after 50 min of light illumination, (D) comparison of the CH_4 yield generated using different catalysts under simulated solar light, and (E) plausible reaction mechanism for CO_2 conversion using Cu–TiO_2-*x*. (reproduced from ref. 81 with permission from the Royal Society of Chemistry, copyright 2015).

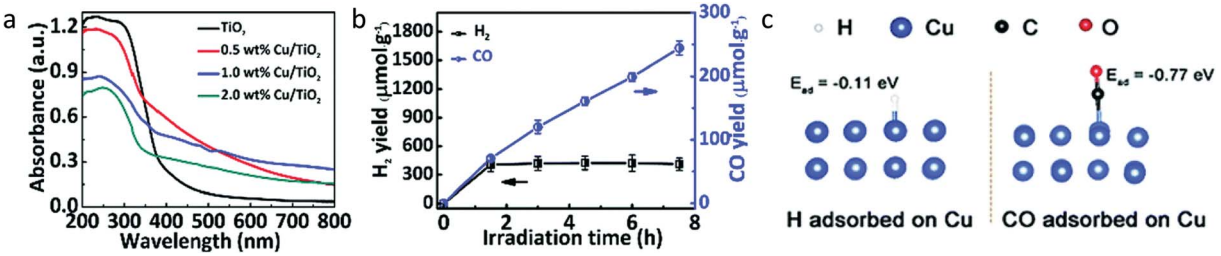

Fig. 25 (a) UV-vis DRS of different samples, (b) time profile for the generation of products, CO and H_2 using 0.5 wt% Cu/TiO_2 photocatalyst, and (c) by use of DFT, calculation of adsorption energy of H_2 and CO on the Cu surface (reproduced from ref. 82 with permission from the Royal Society of Chemistry, copyright 2019).

of hydrogen evolution. However, the yield of CO generation was found to decrease in a sample having a Cu content more than 1 wt%. This was due to the aggregation of Cu and the light-shielding caused by the presence of excess Cu on the surface.

The generation of oxygen defects after heteroatom doping into the TiO_2 lattice and its effect on photocatalytic CO_2 conversion were studied by Pham *et al.*[83] They synthesized Ag and Cu co-doped TiO_2 over honeycombed structured polyurethane (referred to as Ag@Cu–TiO_2/PU). Co-doping with 2 wt% Ag and 4 wt% Cu (referred to as 2Ag@4Cu/TiO_2/PU) resulted in a higher Ti^{3+}/Ti^{4+} ratio than the single doped Ag or Cu (6 wt% Ag or Cu@TiO_2/PU). This indicated that the co-doping of Ag and Cu further enhanced Ti^{3+} and oxygen vacancies, as evident from XPS analysis. Enhanced absorption of visible light, separation of the electron and hole and adsorption of CO_2 due to the presence of defects resulted in the enhancement of the total photocatalytic yield of 2Ag@4Cu/TiO_2/PU under visible light illumination. The total product yield of CH_4 and CO was found to be 880 and 550 μmol g^{-1} in 6 h using 2Ag@4Cu/TiO_2/PU, respectively. They also observed a slight improvement in the CH_4 and CO production yield at a rate of 933 and 588 μmol g^{-1} in 6 h using co-doped 2 wt% Cu and 4 wt% V–TiO_2/PU under visible light illumination.[84]

Similarly, Wang *et al.*[85] synthesized cobalt doped ordered mesoporous TiO_2 by a multicomponent self-assembly process (referred to as Co–OMT-*x*, OMT stands for ordered mesoporous TiO_2; the molar ratio of Co/Ti varied from 0.002 to 0.2; $x = 1$–8 corresponds to molar ratio of Co/Ti 0.002, 0.005, 0.01, 0.025, 0.05, 0.10, 0.15, and 0.20). The maximum CO_2 conversion was found at 0.025 molar ratio of Co/Ti, with a yield of CO and CH_4 at a rate of 1.94 and 0.09 μmol g^{-1} h^{-1}, respectively (Fig. 26a). The greater selectivity for CH_4 formation was observed when the molar ratio of Co/Ti was 0.2. This improvement in selectivity with an increase in the Co content was attributed to the formation of the nanocomposite of Co_3O_4/doped Co–TiO_2 and increase in oxygen vacancies. As a result of doping of Co, the CB

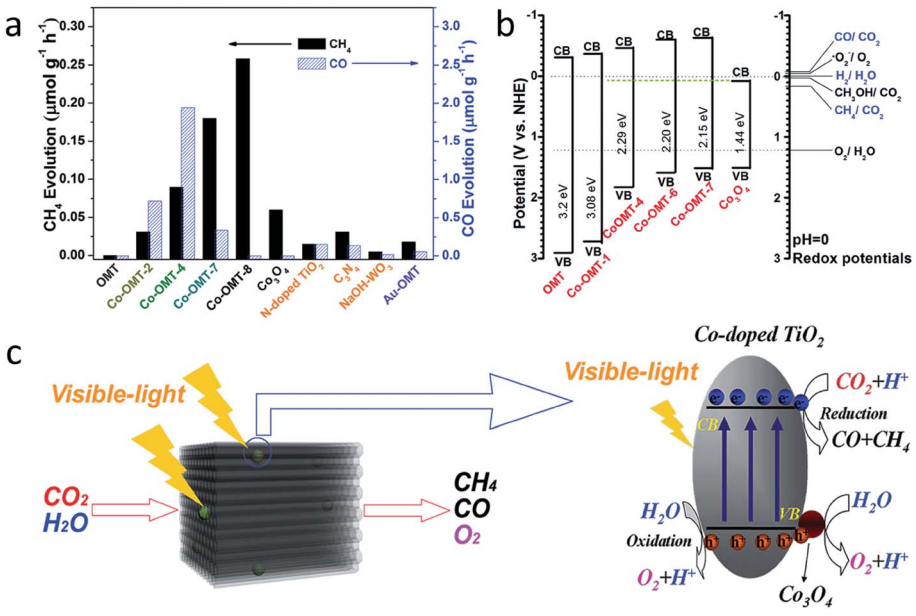

Fig. 26 (a) Comparison of photocatalytic CO_2 conversion using different samples, (b) valence band and conduction band position in different samples, (c) schematic representation of photocatalytic CO_2 conversion over Co-doped mesoporous ordered TiO_2 (reproduced from ref. 85 with permission from the Royal Society of Chemistry, copyright 2015).

and VB shifted upward, resulting in the decrease in bandgap with an increase in Co content as shown in Fig. 26b. Fig. 26c shows the schematic illustration of the proposed mechanism for CO_2 conversion.

Different precursors of Ti can be used for the generation of inherent oxygen vacancies. Yaghoubi *et al.*[86] synthesized TiO_2 using the peroxo-titanium complex and found the generation of defects during the synthesis. The obtained crystalline TiO_2 was composed of a mixed phase of anatase, rutile and brookite. The VB and CB of mixed-phase TiO_2 were determined with the help of UPS and inverse photoemission spectroscopy (IPES), respectively (Fig. 27a and b). The bandgap determined by the above two techniques was 3.8 eV higher than that determined using DRS (3.1 eV as depicted in Fig. 27c) due to the high threshold energy required to create an unbound e^- and h^+ pair. UPS spectra show that the edge corresponds to midgap states at 1.7 eV below the Fermi level *i.e.* at 2.2 eV from the conduction band edge, which was also elucidated by the Urbach tail in the UV-visible DRS spectrum (Fig. 27c). XPS and ICP-OES were performed to rule out the possibility of extended absorption due to doping with heteroatoms. The formation of the mid-gap states within the bandgap was due to the presence of oxygen defects and Ti^{3+} and not because of heteroatom doping. The presence of midgap states was responsible for the absorption in the visible region. The mechanism for photocatalytic CO_2 conversion was proposed (Fig. 27d), where illumination of the TiO_2 with the photon of energy equal to and greater than 2.2 eV excited the electron from midgap state to the CB where the reduction of CO_2 takes place. The hole in the mid-gap states oxidizes water to give a proton. The catalyst was active for CO_2 conversion under both solar light and visible light illumination. The mixed-phase TiO_2 showed CO and CH_4 yield at a rate of 1357 and 360 ppm g^{-1} in 6 h under visible light illumination, which was 6.75 and 7.66 times better as compared to P25 TiO_2, respectively. The total quantum yield was found to be of 0.0289% in the region of 250–564 nm.

Han *et al.*[87] synthesized the defective truncated bi-pyramidal structure with co-exposed {101} and {001} facets of anatase TiO_2 (referred to as TiO_2–B) using TiB_2 as the precursor by one-step hydrothermal treatment. To further improve the charge separation, nanosheets of SnS_2 were loaded over defective TiO_2–B (referred to as SnS_2/TiO_2–B). XPS studies indicated that the

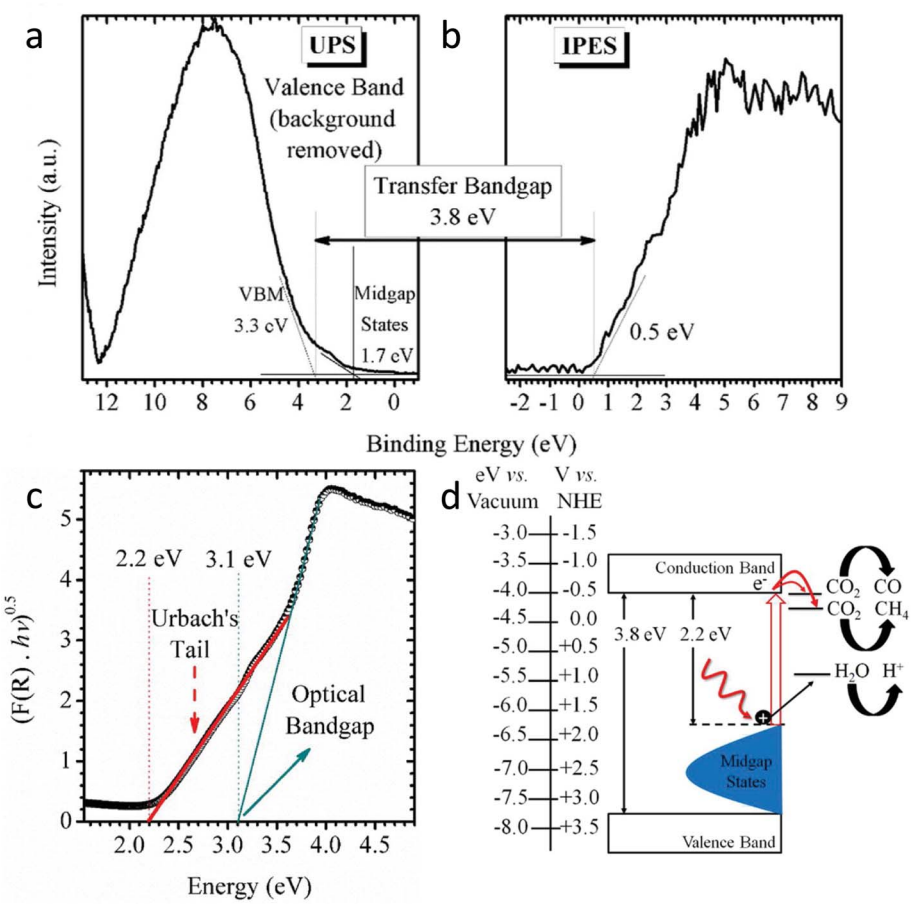

Fig. 27 Valence band and conduction band of TiO_2 nanoparticles determined using (a) UPS and (b) IPES spectra and (c) plot of Kubelka–Munk Function *vs.* energy derived from the UV-visible DRS spectrum of TiO_2. The green line denotes the optical bandgap, whereas the red line shows Urbach's tail. (d) Schematic representation of the electronic structure of TiO_2 in combination with a suggested diagram for photocatalytic CO_2 conversion. The blue region shows the presence of extended localized states within the bandgap resulting in the absorption in the visible region (reproduced from ref. 86 with permission from the American Chemical Society, copyright 2015).

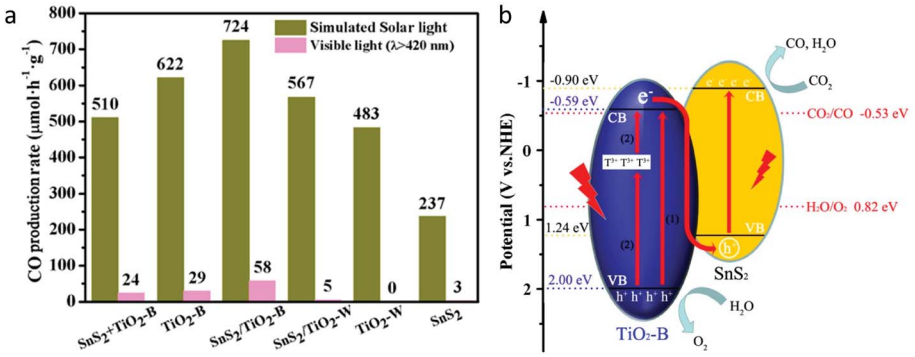

Fig. 28 (a) Comparison of the yield of CO produced by photocatalytic CO_2 conversion using SnS_2/TiO_2–B under simulated solar light and visible light and (b) schematic for the Z-scheme mechanism of separation of photogenerated charge carriers (reproduced from ref. 87 with permission from MDPI, copyright 2019).

oxygen vacancies were maintained well even after the formation of the composite with SnS_2 nanosheets. The improved light absorption and adsorption and activation of the CO_2 molecule due to the presence of defects in TiO_2 and enhanced separation of charge carriers as a result of the formation of the Z-scheme heterojunction between TiO_2 and SnS_2 nanosheets improved the photocatalytic performance of the sample. The highest CO production was observed at a rate of 58 μmol g^{-1} h^{-1} with a selectivity of 96.3% under visible light irradiation (Fig. 28a). In the Z-scheme mechanism, the electron from the CB of TiO_2–B gets transferred to the hole in the VB of SnS_2 (Fig. 28b). The electron present in the CB of SnS_2 was then used for the conversion of the CO_2 to CO.

Another strategy adopted by Shi *et al.*[88] was to construct a heterojunction between TiO_2 and g-C_3N_4 to separate the photogenerated charge carriers and improve the activity. They synthesized the 0D/2D heterojunctions of oxygen defect rich TiO_2/g-C_3N_4 (referred to as $y$$TiO_{2-x}$–MCN) by *in situ* two-step pyrolysis of NH_2-MIL-125(Ti) and melamine. HR-TEM images revealed that the 5 nm quantum dots of TiO_2 were homogeneously distributed on the surface of the nanosheets of g-C_3N_4. XPS and EPR showed the existence of Ti^{3+} and oxygen vacancies in $y$$TiO_{2-x}$–MCN. The *g*-value for the unpaired electron of g-C_3N_4 and oxygen vacancies of TiO_2 is similar. On comparison of the EPR spectra of the TiO_2–MCN (synthesized by one-step pyrolysis mixing of TiO_2 and melamine), which was devoid of oxygen vacancies, MCN (g-C_3N_4 synthesized by thermal pyrolysis of melamine) and $y$$TiO_{2-x}$–MCN revealed that the increase in intensity in $y$$TiO_{2-x}$–MCN could be attributed to the existence of oxygen defects of TiO_2 rather than an unpaired electron in g-C_3N_4. The charge transfer that occurs from 2D-g-C_3N_4 to 0D-TiO_2 in less than 1 ps was revealed by the transient photoluminescence and femtosecond and nanosecond pumped-probe transient absorption spectra. CO_2 adsorption of $y$$TiO_{2-x}$–MCN (8–10 cm^3 g^{-1}) was ten times higher than that of MCN (0.8 cm^3 g^{-1}). The presence of oxygen defects enhanced both absorption of light in the visible region and the CO_2 adsorption. The photocatalytic performance was studied in the presence of an acetonitrile/triethanolamine mixture and $Co(bpy)_3^{2+}$ as the cocatalyst in the presence of visible light. CO generation at a rate of 388.9 μmol g^{-1} using $2TiO_{2-x}$/MCN was observed to be five times higher than that of MCN (75.3 μmol g^{-1}) in 5 h. The significant improvement in activity of TiO_{2-x}/MCN was attributed to the enhanced visible light absorption, CO_2 adsorption, large surface area and efficient charge separation due to the formation of an interface between TiO_2 and g-C_3N_4. After absorption of light, the electron from g-C_3N_4 transfers to the conduction band of TiO_{2-x} where the conversion of CO_2 to CO takes place in the presence of the electron mediator $Co(bpy)_3^{2+}$. A hole is generated on TiO_{2-x} transfer to g-C_3N_4 where it gets removed by oxidation of triethanolamine, and this efficient transfer of the electron and hole pair across the heterojunction resulted in the effective separation of charge carriers.

Feng *et al.*[89] reported the formation of Ti^{3+} ions while depositing the MgO layer over porous TiO_2 by atomic layer deposition (ALD). Porous TiO_2 was synthesized using the metal–organic framework MIL-125 as the Ti precursor. Five layers of MgO deposited by the ALD showed four times higher photocatalytic yield than porous TiO_2 and 21 times better than P25. Uniform distribution of MgO over porous TiO_2 generated the active site for CO_2 reduction by increasing the amount of Ti^{3+} species on the surface and hydroxyl groups bonded to Mg and also helped in reduction of the surface photogenerated charge recombination rate by passivating the surface states of porous TiO_2. With an increase in ALD cycles to more than five, photocatalytic activity for CO generation decreased due to the reduced contact of adsorbed CO_2 with TiO_2. The photocatalytic activity was found to be higher for the ALD deposited MgO than that from the wet impregnation (WI) method. This was due to the high concentration of Ti^{3+} and oxygen defects in the case of MgO deposited by the ALD method.

7. Conclusions and future directions

The defect engineering in TiO_2 has raised tremendous interest in the scientific community and different protocols based on reduction and oxidation strategies have been introduced for the synthesis of oxygen vacant/Ti^{3+} induced TiO_2. This review discussed various ways for the introduction of defects such as oxygen vacancies and Ti^{3+} generation and their impact on

photocatalytic CO_2 conversion. The formation of the disordered layer and concentration of defects play an important role in determining the product yield and selectivity in photocatalytic CO_2 conversion. Defects significantly narrowed the bandgap, which resulted in improved absorption in the visible region. In addition, the defects provided the sites to bind and activate the CO_2 into $CO_2^{\bullet-}$, which is much easier to reduce further and thus enhance the CO_2 conversion yield.

The point defects in TiO_2 were generated by different synthesis methods such as treatment under a hydrogen atmosphere, inert gas (Ar, He, or N_2), using a reducing agent, hydrogen plasma treatment, metallothermic reduction, doping with a heteroatom, *etc.* Although there are different methods reported in the literature, several of them required harsh conditions, hazardous chemicals, and costly and complex procedures or equipment. Therefore, the development of a low temperature, cost-effective and scalable process is needed for its practical application.

Thermal treatment in the presence of hydrogen gas at ambient pressure was found to be useful not only for the generation of defects but also to reduce the metal ion into metal nanoparticles and also to clean the surface of the catalyst. Also, it was observed that the product yield and selectivity depend on the particle size and degree of hydrogenation. Smaller particles of TiO_2 dispersed over the silica support showed a higher degree of reduction than the large particles. It was also observed that the presence of an oxygen vacancy could alter the dispersion of metal nanoparticles and thus affect the photo-thermo-catalytic activity. The decoration of the surface of the defective TiO_2 with chemical species like thiocyanate passivates the defects and also induces the electric field at the interface, which helped in the separation of charge carriers.

Defect generation using hydrides like $NaBH_4$ is one of the safe and easiest ways for the generation of a reductive atmosphere. Also, the generation of defects in the presence of He, N_2, Ar and vacuum was also reported. The concentration of vacancies generated after thermal treatment in an inert atmosphere was dependent on the partial pressure of oxygen. By using the flame reduction method, defects can be induced within a minute because of the faster heating rate and high temperature of the flame. The metallothermic reduction method is a cost-effective method as compared to the high pressure and temperature hydrogenation method. In this method, metals such as Al, Mg, Li and Zn were used as a reducing agent to capture lattice oxygen effectively. By using lithiothermic reduction, defects can be generated at room temperature.

In all the reduction methods, the concentration of defects was found to increase with an increase in the amount of reducing agent. Also, the enhancement in light absorption was observed with an increase in the concentration of defects. But a similar trend was not observed for the photocatalytic activity. Hence the optimum amount of defects is needed to get a better yield.

Along with the defects, the presence of particular facets was also found to impact the CO_2 conversion yield. Facet engineering was found to be effective for the separation of charge carriers at different facets. Shi *et al.*[77] generated disorder layers only on particular facets using mild reducing conditions and found that the chemical reactions on the facets were altered. The holes are supposed to accumulate at the {001} surface, but they observed that due to the formation of the electron-rich defective layer, the reduction of CO_2 occurred over the {001} facets and oxidation over the {101} facets. Along with the generation of oxygen vacancies or Ti^{3+} in TiO_2, attempts were also made to improve the charge carrier separation by facet selective deposition of metal nanoparticles, doping with heteroatoms like Co, Cu, *etc.*, Z-scheme heterojunction formation with visible light active semiconductors like SnS_2 and g-C_3N_4, and surface decoration with chemical species like thiocyanate, which helped induce an electric field and passivated the surface defects.

This review also discusses the theoretical aspects of the formation of different products. Theoretical studies revealed that the formaldehyde pathway is most preferred in the case of both defective and non-defective TiO_2, while the carbene pathway is not favored over the defective TiO_2 due to the formation of energetically unfavourable $^{\bullet}C$ intermediates.

The photocatalytic CO_2 conversion yield of defective TiO_2 is summarized in Table 1. It is difficult to compare the yield as the reaction conditions reported by the different research groups were different. Also, the expression of the product yield in terms of $\mu mol\ g^{-1}\ h^{-1}$ is inappropriate as it does not account for the intensity of the light source, photons falling on the reactor system, illumination area, *etc.* Also, it is difficult to extrapolate the yield in terms of per gram of catalyst as the yield does not vary linearly with the catalyst amount. Catalyst dispersion also plays a crucial role in determining the yield of the product.

There are several unknowns and challenges not yet addressed in this field. The nature and concentration of the defects and how they are helping in the improvement of photocatalytic activity are still not well understood. The defects created by adopting different synthetic methods have different physical and chemical properties and thus, assessment of the exact reason responsible for the enhancement of photocatalytic activity is another challenge. More information on structural distortion needs to be acquired using various *in situ* spectroscopy techniques. This will be helpful to rationalize the design of the photocatalyst. Efforts to produce C_2 and higher products by utilizing the advantages provided by the defects present on the surface of TiO_2 are needed. Recent work by Chen *et al.*[90] who reported the activation of CO_2 over defective Bi_2O_3 for the production of the dimethyl carbonate using methanol, and Polshettiwar *et al.*[91] who reported activation of CO_2 using defective dendritic fibrous nanosilica (DFNS) without any metal sites, could be a way forward for defect engineering in other catalytic materials.

The catalyst's stability is another critical issue as the strong adsorption of the intermediate species at defect sites may deactivate the catalyst. Adsorption of reactants and desorption of products are important factors. Therefore, the removal of the products generated during the reaction is necessary to further prevent their oxidation into CO_2 or other products by accepting a hole. One of the ways to improve the adsorption and desorption kinetics is by carrying out the photothermal reactions where the CO_2 conversion can be performed at a slightly higher temperature than room temperature. The high temperature may hamper the adsorption of CO_2, but temperature

optimization can result in the desired results where desorption as well as adsorption could be possible.

Along with tailoring of defects in TiO_2, designing a specific photoreactor is also equally important in the view of efficient removal of the products as well as effective utilization of light falling on the system. A monolith photoreactor design holds promise for better product yields.[92]

Overall, defect engineering in TiO_2 is a potential approach for the production of value-added products and chemicals from photocatalytic CO_2 conversion by utilizing solar energy.

Conflicts of interest

There are no conflicts to declare.

Acknowledgements

We acknowledge the funding support of the Department of Atomic Energy (under project no. R&D-TIFR-RTI4003) and Mission Innovation India, Department of Science & Technology, Government of India.

References

1 T. Kong, Y. Jiang and Y. Xiong, Photocatalytic CO_2 conversion: What can we learn from conventional COx hydrogenation?, *Chem. Soc. Rev.*, 2020, **49**, 6579–6591.
2 M. Meinshausen, N. Meinshausen, W. Hare, S. C. B. Raper, K. Frieler, R. Knutti, D. J. Frame and M. R. Allen, Greenhouse-gas emission targets for limiting global warming to 2 °C, *Nature*, 2009, **458**, 1158–1162.
3 M. Khalil, J. Gunlazuardi, T. A. Ivandini and A. Umar, Photocatalytic conversion of CO_2 using earth-abundant catalysts: A review on mechanism and catalytic performance, *Renew. Sust. Energ. Rev*, 2019, **113**, 109246.
4 Y. Zhang, B. Xia, J. Ran, K. Davey and S. Z. Qiao, Atomic-level reactive sites for semiconductor-based photocatalytic CO_2 reduction, *Adv. Energy Mater.*, 2020, **10**, 1903879.
5 X. Chang, T. Wang and J. Gong, CO_2 photo-reduction: insights into CO_2 activation and reaction on surfaces of photocatalysts, *Energy Environ. Sci.*, 2016, **9**, 2177–2196.
6 J. Albero, Y. Peng and H. García, Photocatalytic CO_2 reduction to C2+ products, *ACS Catal.*, 2020, **10**(10), 5734–5749.
7 S. R. Lingampalli, M. M. Ayyub and C. N. R. Rao, Recent progress in the photocatalytic reduction of carbon dioxide, *ACS Omega*, 2017, **2**, 2740–2748.
8 T. P. Nguyen, D. L. T. Nguyen, V. H. Nguyen, T.-H. Le, D.-V. N. Vo, Q. T. Trinh, S.-R. Bae, S. Y. Chae, S. Y. Kim and Q. V. Le, Recent Advances in TiO_2-Based photocatalysts for reduction of CO_2 to fuels, *Nanomaterials*, 2020, **10**, 337.
9 S. Sato, T. Arai and T. Morikawa, Toward solar-driven photocatalytic CO_2 reduction using water as an electron donor, *Inorg. Chem.*, 2015, **54**, 5105–5113.
10 M. Halmann, Photoelectrochemical reduction of aqueous carbon dioxide on p-type gallium phosphide in liquid junction solar cells, *Nature*, 1978, **275**, 115–116.
11 T. Inoue, A. Fujishima, S. Konishi and K. Honda, Photoelectrocatalytic reduction of carbon dioxide in aqueous suspensions of semiconductor powders, *Nature*, 1979, **277**, 637–638.
12 J. Schneider, M. Matsuoka, M. Takeuchi, J. Zhang, Y. Horiuchi, M. Anpo and D. W. Bahnemann, Understanding TiO_2 photocatalysis: Mechanisms and materials, *Chem. Rev.*, 2014, **114**(19), 9919–9986.
13 J. Low, L. Zhang, B. Zhu, Z. Liu and J. Yu, TiO2 photonic crystals with localized surface photothermal effect and enhanced photocatalytic CO2 reduction activity, *ACS Sustainable Chem. Eng.*, 2018, **6**, 15653–15661.
14 A. Meng, L. Zhang, B. Cheng and J. Yu, TiO2–MnOx–Pt hybrid multiheterojunction film photocatalyst with enhanced photocatalytic CO_2-reduction activity, *ACS Appl. Mater. Interfaces*, 2019, **11**, 5581–5589.
15 F. Xu, B. Zhu, B. Cheng, J. Yu and J. Xu, 1D/2D TiO2/MoS2 hybrid nanostructures for enhanced photocatalytic CO2 reduction, *Adv. Opt. Mater.*, 2018, **6**(23), 1800911.
16 D. Gao, X. Wu, P. Wang, Y. Xu, H. Yu and J. Yu, Simultaneous realization of direct photoinduced deposition and improved H_2-evolution performance of Sn-nanoparticle-modified TiO2 photocatalyst, *ACS Sustainable Chem. Eng.*, 2019, **7**, 10084–10094.
17 X. Chen and S. S. Mao, Titanium dioxide nanomaterials: Synthesis, properties, modifications, and applications, *Chem. Rev.*, 2007, **107**, 2891–2959.
18 R. Asahi, T. Morikawa, T. Ohwaki, K. Aoki and Y. Taga, Visible light photocatalysis in nitrogen-doped titanium oxides, *Science*, 2001, **293**, 269–271.
19 S. G. Kumar and L. G. Devi, Review on modified TiO_2 photocatalysis under UV/Visible light: Selected results and related mechanisms on interfacial charge carrier transfer dynamics, *J. Phys. Chem. A*, 2011, **115**(46), 13211–13241.
20 M. Nasr, C. Eid, R. Habchi, P. Miele and M. Bechelany, Recent progress on titanium dioxide nanomaterials for photocatalytic applications, *ChemSusChem*, 2018, **11**(18), 3023–3047.
21 S. Xie, H. Zhang, G. Liu, X. Wu, J. Lin, Q. Zhang and Y. Wang, Tunable localized surface plasmon resonances in MoO_{3-x}-TiO_2 nanocomposites with enhanced catalytic activity for CO2 photoreduction under visible light, *Chinese*, *J. Catal.*, 2020, **41**(7), 1125–1131.
22 F. Xu, K. Meng, B. Cheng, S. Wang, J. Xu and J. Yu, Unique S-scheme heterojunctions in self-assembled TiO_2/$CsPbBr_3$ hybrids for CO_2 photoreduction, *Nat. Commun.*, 2020, **11**, 4613.
23 A. Li, T. Wang, X. Chang, Z.-J. Zhao, C. Li, Z. Huang, P. Yang, G. Zhou and J. Gong, Tunable syngas production from photocatalytic CO2 reduction with mitigated charge recombination driven by spatially separated cocatalysts, *Chem. Sci.*, 2018, **9**(24), 5334–5340.

24 Y. Xia and J. Yu, Reaction: Rational Design of Highly Active Photocatalysts for CO_2 Conversion, *Chem*, 2020, **6**(5), 1039–1040.

25 M.-Q. Yang and Y.-J. Xu, Photocatalytic conversion of CO_2 over graphene-based composites: current status and future perspective, *Nanoscale Horiz.*, 2016, **1**, 185–200.

26 K.-Q. Lu, Y.-H. Li, F. Zhang, M.-Y. Qi, X. Chen, Z.-R. Tang, Y. M. A. Yamada, M. Anpo, M. Conte and Y.-J. Xu, Rationally designed transition metal hydroxide nanosheet arrays on graphene for artificial CO_2 reduction, *Nat. Commun.*, 2020, **11**, 5181.

27 X. Pan and Y.-J. Xu, Defect-Mediated Growth of Noble-Metal (Ag, Pt, and Pd) Nanoparticles on TiO_2 with Oxygen Vacancies for Photocatalytic Redox Reactions under Visible Light, *J. Phys. Chem. C*, 2013, **117**, 17996–18005.

28 L. Yuan, K.-Q. Lu, F. Zhang, X. Fu and Y.-J. Xu, Unveiling the interplay between light-driven CO2 photocatalytic reduction and carbonaceous residues decomposition: A case study of Bi_2WO_6-TiO_2 binanosheets, *Appl. Catal., B*, 2018, **237**, 424–431.

29 L. Yuan and Y.-J. Xu, Photocatalytic conversion of CO_2 into value-added and renewable fuels, *Appl. Surf. Sci.*, 2015, **342**, 154–167.

30 K. Nakata and A. Fujishima, TiO_2 photocatalysis: Design and applications, *J. Photochem. Photobiol., C*, 2012, **13**(3), 169–189.

31 X. Chen, L. Liu and F. Huang, Black titanium dioxide (TiO_2) nanomaterials, *Chem. Soc. Rev.*, 2015, **44**, 1861–1885.

32 A. Chatzitakis and S. Sartori, Recent advances in the use of black TiO_2 for production of hydrogen and other solar fuels, *ChemPhysChem*, 2019, **20**, 1–11.

33 X. Pan, M.-Q. Yang, X. Fu, N. Zhang and Y.-J. Xu, Defective TiO_2 with oxygen vacancies: synthesis, properties and photocatalytic applications, *Nanoscale*, 2013, **5**, 3601–3614.

34 B. B. Adormaa, W. K. Darkwah and Y. Ao, Oxygen vacancies of the TiO_2 nano-based composite photocatalysts in visible light responsive photocatalysis, *RSC Adv.*, 2018, **8**, 33551–33563.

35 X. Chang, T. Wang and J. Gong, CO_2 Photo-reduction: Insights into CO_2 Activation and Reaction on Surfaces of Photocatalysts, *Energy Environ. Sci.*, 2016, **9**, 2177–2196.

36 X. B. Chen, L. Liu, P. Y. Yu and S. S. Mao, Increasing solar absorption for photocatalysis with black hydrogenated titanium dioxide nanocrystals, *Science*, 2011, **331**, 746.

37 A. Naldoni, M. Altomare, G. Zoppellaro, N. Liu, S. Kment, R. Zboril and P. Schmuki, Photocatalysis with reduced TiO_2: From black TiO_2 to cocatalyst- free hydrogen production, *ACS Catal.*, 2019, **9**, 345–364.

38 T. L. Thompson and J. T. Yates Jr, TiO_2-based photocatalysis: surface defects, oxygen and charge transfer, *Top. Catal.*, 2005, **35**, 3–4.

39 K. K. Adepalli, M. Kelsch, R. Merkle and J. Maier, Influence of line defects on the electrical properties of single crystal TiO_2, *Adv. Funct. Mater.*, 2013, **23**, 1798–1806.

40 H. Zhao, F. Pan and Y. Li, A review on the effects of TiO_2 surface point defects on CO_2 photoreduction with H_2O, *J. Materiomics*, 2017, **3**, 17–32.

41 L.-B. Xiong, J.-L. Li, B. Yang and Y. Yu, Ti^{3+} in the surface of titanium dioxide: generation, properties and photocatalytic application, *J. Nanomater.*, 2012, **2012**, 831524.

42 T. L. Thompson, O. Diwald and J. T. Yates, CO_2 as a Probe for monitoring the surface defects on TiO_2 (110) temperature-programmed desorption, *J. Phys. Chem. B*, 2003, **107**(42), 11700–11704.

43 S. Huygh, A. Bogaerts and E. C. Neyts, How oxygen vacancies activate CO_2 dissociation on TiO_2 anatase (001), *J. Phys. Chem. C*, 2016, **120**(38), 21659–21669.

44 J. Lee, D. C. Sorescu and X. Deng, Electron-induced dissociation of CO_2 on TiO_2 (110), *J. Am. Chem. Soc.*, 2011, **133**, 10066–10069.

45 S. Tan, Y. Zhao, J. Zhao, Z. Wang, C. Ma, A. Zhao, B. Wang, Y. Luo, J. Yang and J. Hou, CO_2 dissociation activated through electron attachment on the reduced rutile TiO2 (110)-1×1 surface, *Phys. Rev. B*, 2011, **84**, 155418.

46 F. M. Hossain and G. E. Murch, The effect of defect disorder on the electronic structure of rutile TiO_{2-x}, *Defect Diffus. Forum*, 2006, **251–252**, 1–12.

47 A. Razzaq and S.-I. In, TiO_2 based nanostructures for photocatalytic CO_2 conversion to valuable chemicals, *Micromachines*, 2019, **10**(5), 326.

48 Y. Ji and Y. Luo, New mechanism for photocatalytic reduction of CO_2 on the anatase TiO_2 (101) surface: the essential role of oxygen vacancy, *J. Am. Chem. Soc.*, 2016, **138**(49), 15896–15902.

49 J.-Y. Liu, X.-Q. Gong and A. N. Alexandrova, Mechanism of CO_2 photocatalytic reduction to methane and methanol on defective anatase TiO_2 (101): A Density Functional Theory Study, *J. Phys. Chem. C*, 2019, **123**, 3505–3511.

50 X. Liu, G. Zhu, X. Wang, X. Yuan, T. Lin and F. Huang, Progress in black titania: A new material for advanced photocatalysis, *Adv. Energy Mater.*, 2016, **6**(17), 1600452.

51 J. Liu, B. Liu, Y. Ren, Y. Yuan, H. Zhao, H. Yang and S. F. Liu, Hydrogenated nanotubes/nanowires assembled from TiO_2 nanoflakes with exposed {111} facets: excellent photocatalytic CO_2 reduction activity and charge separation mechanism between (111) and $(\bar{1}\bar{1}\bar{1})$ polar surfaces, *J. Mater. Chem. A*, 2019, **7**, 14761–14775.

52 X. Xuan, S. Tu, H. Yu, X. Du, Y. Zhao, J. He, H. Dong, X. Zhang and H. Huang, Size-dependent selectivity and activity of CO_2 photoreduction over black nano-titanias grown on dendritic porous silica particles, *Appl. Catal. B*, 2019, **255**, 117768.

53 T. Billo, F.-Y. Fu, P. Raghunath, I. Shown, W.-F. Chen, H.-T. Lien, T.-H. Shen, J.-F. Lee, T.-S. Chan, K.-Y. Huang, C.-I. Wu, M. C. Lin, J.-S. Hwang, C.-H. lee, L.-C. Chen and K.-H. Chen, Ni-Nanocluster Modified Black TiO_2 with Dual Active Sites for Selective Photocatalytic CO_2 Reduction, *Small*, 2018, **14**, 1702928.

54 F.-Y. Fu, I. Shown, C.-S. Li, P. Raghunath, T.-Y. Lin, T. Billo, H.-L. Wu, C.-I. Wu, P.-W. Chung, M.-C. Lin, L.-C. Chen and K.-H. Chen, KSCN-induced interfacial dipole in black TiO_2 for enhanced photocatalytic CO_2 reduction, *ACS Appl. Mater. Interfaces*, 2019, **11**(28), 25186–25194.

55 J. Ye, J. He, S. Wang, X. Zhou, Y. Zhang, G. Liu and Y. Yang, Nickel-loaded black TiO_2 with inverse opal structure for photocatalytic reduction of CO_2 under visible light, *Sep. Purif. Technol.*, 2019, **220**, 8–15.

56 L. Liu, F. Gao, H. Zhao and Y. Li, Tailoring Cu valence and oxygen vacancy in Cu/TiO_2 catalysts for enhanced CO_2 photoreduction efficiency, *Appl. Catal. B*, 2013, **134–135**, 349–358.

57 Y. Li, C. Wang, M. Song, D. Li, X. Zhang and Y. Liu, TiO_{2-x}/CoO_x photocatalyst sparkles in photothermocatalytic reduction of CO_2 with H_2O steam, *Appl. Catal. B*, 2019, **243**, 760–770.

58 P. Martelli, R. Caputo, A. Remhof, P. Mauron, A. Borgschulte and A. Züttel, Stability and Decomposition of $NaBH_4$, *J. Phys. Chem. C*, 2010, **114**, 7173–7177.

59 S. Sorcar, Y. Hwang, C. A. Grimes and S.-I., Highly enhanced and stable activity of defect-induced titania nanoparticles for solar light-driven CO_2 reduction into CH_4, *Mater. Today*, 2017, **20**, 507–515.

60 S. Sorcar, J. Thompson, Y. Hwang, Y. H. Park, T. Majima, C. A. Grimes, J. R. Durrant and S.-I. In, High-rate solar-light photoconversion of CO_2 to fuel: controllable transformation from C_1 to C_2 products, *Energy Environ. Sci.*, 2018, **11**, 3183–3193.

61 S. Sorcar, Y. Hwang, J. Lee, H. Kim, K. M. Grimes, C. A. Grimes, J.-W. Jung, C.-H. Cho, T. Majima, M. R. Hoffmann and S.-I. In, CO_2, water, and sunlight to hydrocarbon fuels: a sustained sunlight to fuel (Joule-to-Joule) photoconversion efficiency of 1%, *Energy Environ. Sci.*, 2019, **12**, 2685–2696.

62 Y. Yan, M. Han, A. Konkin, T. Koppe, D. Wang, T. Andreu, G. Chen, U. Vetter, J. R. Morante and P. Schaaf, Slightly hydrogenated TiO_2 with enhanced photocatalytic performance, *J. Mater. Chem. A*, 2014, **2**, 12708–12716.

63 L. Liu, H. Zhao, J. M. Andino and Y. Li, Photocatalytic CO_2 Reduction with H_2O on TiO_2 Nanocrystals: Comparison of Anatase, Rutile, and Brookite Polymorphs and Exploration of Surface Chemistry, *ACS Catal.*, 2012, **2**(8), 1817–1828.

64 X. Xin, T. Xu, L. Wang and C. Wang, Ti^{3+}-self doped brookite TiO_2 single-crystalline nanosheets with high solar absorption and excellent photocatalytic CO_2 reduction, *Sci. Rep.*, 2016, **6**, 23684.

65 J. Zhao, Y. Li, Y. Zhu, Y. Wang and C. Wang, Enhanced CO_2 photoreduction activity of black TiO_2−coated Cu nanoparticles under visible light irradiation: Role of metallic Cu, *Appl. Catal., A*, 2016, **510**, 34–41.

66 P. Kar, S. Zeng, Y. Zhang, E. Vahidzadeh, A. Manuel, R. Kisslinger, K. M. Alam, U. K. Thakur, N. Mahdi, P. Kumar and K. Shankar, High rate CO_2 photoreduction using flame annealed TiO_2 nanotubes, *Appl. Catal., B*, 2019, **243**, 522–536.

67 W. Tu, Y. Zhou, Q. Liu, S. Yan, S. Bao, X. Wang, M. Xiao and Z. Zou, An in Situ simultaneous reduction-hydrolysis technique for fabrication of TiO_2 -graphene 2D sandwich-like hybrid nanosheets: graphene-promoted selectivity of photocatalytic-driven hydrogenation and coupling of CO_2 into methane and ethane, *Adv. Funct. Mater.*, 2013, **23**, 1743–1749.

68 A. Vignes, *Metallurgical Thermochemistry in Extractive Metallurgy 1: Basic Thermodynamics and Kinetics*, John Wiley & Sons, Inc., USA, 2013.

69 G. Yin, Q. Bi, W. Zhao, J. Xu, T. Lin and F. Huang, Efficient Conversion of CO_2 to Methane Photocatalyzed by Conductive Black Titania, *ChemCatChem*, 2017, **9**, 4389–4396.

70 J. Gao, Q. Shen, R. Guan, J. Xue, X. Liu, H. Jia, Q. Li and Y. Wu, Oxygen vacancy self-doped black TiO_2 nanotube arrays by aluminothermic reduction for photocatalytic CO_2 reduction under visible light illumination, *J. CO2 Util.*, 2020, **35**, 205–215.

71 G. Ou, Y. Xu, B. Wen, R. Lin, B. Ge, Y. Tang, Y. Liang, C. Yang, K. Huang, D. Zu, R. Yu, W. Chen, J. Li, H. Wu, L.-M. Liu and Y. Li, Tuning Defects in Oxides at Room Temperature by Lithium Reduction, *Nat. Commun.*, 2018, **9**, 1302.

72 C. Wang, J. Yang, T. Li, Z. Shen, T. Guo, H. Zhang and Z. Lu, In Situ Tuning of Defects and Phase Transition in Titanium Dioxide by Lithiothermic Reduction, *ACS Appl. Mater. Interfaces*, 2020, **12**(5), 5750–5758.

73 K. Sasan, F. Zuo, Y. Wang and P. Feng, Self-doped Ti^{3+}–TiO_2 as a photocatalyst for the reduction of CO_2 into a hydrocarbon fuel under visible light irradiation, *Nanoscale*, 2015, **7**, 13369–13372.

74 W. Fang, L. Khrouz, Y. Zhou, B. Shen, C. Dong, M. Xing, S. Mishra, S. Daniele and J. Zhang, Reduced {001}-TiO_{2-x} photocatalysts: noble-metal-free CO_2 photoreduction for selective CH_4 evolution, *Phys. Chem. Chem. Phys.*, 2017, **19**, 13875–13881.

75 L. Liu, Y. Jiang, H. Zhao, J. Chen, J. Cheng, K. Yang and Y. Li, Engineering Coexposed {001} and {101} Facets in Oxygen-Deficient TiO_2 Nanocrystals for Enhanced CO_2 Photoreduction under Visible Light, *ACS Catal.*, 2016, **6**, 1097–1108.

76 Y. Liu, C. Miao, P. Yang, Y. He, J. Feng and D. Li, Synergetic promotional effect of oxygen vacancy-rich ultrathin TiO_2 and photochemical induced highly dispersed Pt for photoreduction of CO_2 with H_2O, *Appl. Catal., B*, 2019, **244**, 919–930.

77 D. R. Shi and P. Y. Chen, Controlled Formation of Defective Shell on TiO_2 (001) Facets for Enhanced Photocatalytic CO_2 Reduction, *ChemCatChem*, 2019, **11**, 2270–2276.

78 W. Qingli, Z. Zhaoguo, C. Xudong, H. Zhengfeng, D. Peimei, C. Yi and Z. Xiwen, Photoreduction of CO_2 using black TiO_2 films under solar light, *J. CO2 Util.*, 2015, **12**, 7–11.

79 X. Liu, M. Ye, S. Zhang, G. Huang, C. Li, J. Yu, P. K. Wong and S. Liu, Enhanced photocatalytic CO_2 valorization over TiO_2 hollow microspheres by synergetic surface tailoring and Au decoration, *J. Mater. Chem. A*, 2018, **6**, 24245.

80 G. Yin, X. Haung, T. Chen, W. Zhao, Q. Bi, J. Xu, Y. Han and F. Haung, Hydrogenated Blue Titania for Efficient Solar-to-Chemical Conversions: Preparation, Characterization, and Reaction Mechanism of CO_2 Reduction, *ACS Catal.*, 2018, **8**(2), 1009–1017.

81 S. Zhu, S. Liang, Y. Tong, X. An, J. Long, X. Fu and X. Wang, Photocatalytic reduction of CO_2 with H_2O to CH_4 on Cu(i) supported TiO_2 nanosheets with defective {001} facets, *Phys. Chem. Chem. Phys.*, 2015, **17**, 9761–9770.

82 Y. Lan, Y. Xie, J. Chen, Z. Hu and D. Cui, Selective photocatalytic CO_2 reduction on copper–titanium dioxide: a study of the relationship between CO production and H_2 suppression, *Chem. Commun.*, 2019, **55**, 8068.

83 T.-D. Pham and B.-K. Lee, Novel capture and photocatalytic conversion of CO_2 into solar fuels by metals co-doped TiO_2 deposited on PU under visible light, *Appl. Catal., A*, 2017, **529**, 40–48.

84 T.-D. Pham and B.-K. Lee, Novel photocatalytic activity of Cu@V co-doped TiO_2/PU for CO_2 reduction with H_2O vapor to produce solar fuels under visible light, *J. Catal.*, 2017, **345**, 87–95.

85 T. Wang, X. Meng, G. Liu, K. Chang, P. Li, Q. Kang, L. Liu, M. Li, S. Ouyang and J. Ye, In situ synthesis of ordered mesoporous Co-doped TiO_2 and its enhanced photocatalytic activity and selectivity for the reduction of CO_2, *J. Mater. Chem. A*, 2015, **3**, 9491.

86 H. Yaghoubi, Z. Li, Y. Chen, H. T. Ngo, V. R. Bhethanabolta, B. Joseph, S. Ma, R. Schlaf and A. Takshi, Toward a Visible Light-Driven Photocatalyst: The Effect of Midgap-States-Induced Energy Gap of Undoped TiO_2 Nanoparticles, *ACS Catal.*, 2015, **5**(1), 327–335.

87 A. Han, M. Li, S. Zhang, X. Zhu, J. Han, Q. Ge and H. Wang, Ti^{3+} Defective SnS_2/TiO_2 Heterojunction Photocatalyst for Visible-Light Driven Reduction of CO_2 to CO with High Selectivity, *Catalysts*, 2019, **9**, 927.

88 H. Shi, S. Long, S. Hu, J. Hou, W. Ni, C. Song, K. Li, G. G. Gurzadyan and X. Guo, Interfacial charge transfer in 0D/2D defect-rich heterostructures for efficient solar-driven CO_2 reduction, *Appl. Catal., B*, 2019, **245**, 760–769.

89 X. Feng, F. Pan, H. Zhao, W. Deng, P. Zhang, H.-C. Zhou and Y. Li, Atomic layer deposition enabled MgO surface coating on porous TiO_2 for improved CO_2 photoreduction, *Appl. Catal., B*, 2018, **238**, 274–283.

90 S. Chen, H. Wang, Z. Kang, S. Jin, X. Zhang, X. Zheng, Z. Qi, J. Zhu, B. Pan and Y. Xie, Oxygen vacancy associated single-electron transfer for photofixation of CO_2 to long-chain chemicals, *Nat. Commun.*, 2019, **10**, 788.

91 A. K. Mishra, R. Belgamwar, R. Jana, A. Datta and V. Polshettiwar, *Proc. Natl. Acad. Sci. U. S. A.*, 2020, **117**, 6383–6390.

92 M. Tahir and N. A. S. Amin, Photocatalytic CO_2 reduction and kinetic study over In/TiO_2 nanoparticles supported microchannel monolith photoreactor, *Appl. Catal., A*, 2013, **467**, 483–496.